

Analysis and Characterization of an Unclassified RFI Affecting Ionospheric Amplitude Scintillation Index over the Mediterranean Area

Original

Analysis and Characterization of an Unclassified RFI Affecting Ionospheric Amplitude Scintillation Index over the Mediterranean Area / Pica, Emanuele; Minetto, Alex; Cesaroni, Claudio; Dovis, Fabio. - In: IEEE JOURNAL OF SELECTED TOPICS IN APPLIED EARTH OBSERVATIONS AND REMOTE SENSING. - ISSN 1939-1404. - ELETTRONICO. - 16:(2023), pp. 8230-8248. [10.1109/JSTARS.2023.3267003]

Availability:

This version is available at: 11583/2978034 since: 2023-09-18T06:06:34Z

Publisher:

IEEE

Published

DOI:10.1109/JSTARS.2023.3267003

Terms of use:

This article is made available under terms and conditions as specified in the corresponding bibliographic description in the repository

Publisher copyright

IEEE postprint/Author's Accepted Manuscript

©2023 IEEE. Personal use of this material is permitted. Permission from IEEE must be obtained for all other uses, in any current or future media, including reprinting/republishing this material for advertising or promotional purposes, creating new collecting works, for resale or lists, or reuse of any copyrighted component of this work in other works.

(Article begins on next page)

Analysis and Characterization of an Unclassified RFI Affecting Ionospheric Amplitude Scintillation Index over the Mediterranean Area

Emanuele Pica, Alex Minetto, *Member, IEEE*, Claudio Cesaroni, Fabio Dovis, *Member, IEEE*,

Abstract—Radio Frequency (RF) signals transmitted by Global Navigation Satellite Systems (GNSS) are exploited as signals of opportunity in many scientific activities, ranging from sensing waterways and humidity of the terrain to the monitoring of the ionosphere. The latter can be pursued by processing the GNSS signals through dedicated ground-based monitoring equipment, such as the GNSS Ionospheric Scintillation and Total Electron Content Monitoring (GISTM) receivers. Nonetheless, GNSS signals are susceptible to intentional or unintentional RF interferences (RFIs), which may alter the calculation of the scintillation indices, thus compromising the quality of the scientific data and the reliability of the derived space weather monitoring products. Upon the observation of anomalous scintillation indices computed by a GISTM receiver in the Mediterranean area, the study presents the results of the analysis and characterization of a deliberate, unclassified interferer acting on the L1/E1 GNSS signal bands, observed and captured through an experimental, software defined radio setup. The paper also highlights the adverse impacts of the interferer on the amplitude scintillation indices employed in scientific investigations, and presents a methodology to discriminate among regular and corrupted scintillation data. To support further investigations, a dataset of baseband signals samples affected by the RFI is available at IEEE DataPort.

Index Terms—Radio Frequency Interferences, Ionospheric Scintillations, Remote Sensing, Ionospheric Monitoring, Global Navigation Satellite Systems (GNSS).

I. INTRODUCTION

GNSS signals crossing small scale electron density irregularities in the ionosphere may be subject to rapid fluctuations of their amplitude and phase known as ionospheric scintillations. This is due to the diffractive effects induced on the signals by ionospheric irregularities smaller than the Fresnel scale (few hundred meters for the L-band) [1]–[5]. Ionospheric scintillations may cause cycle slips and loss of lock of the Global Navigation Satellite System (GNSS) signals, thus hindering the accuracy and integrity of precise positioning applications [6]–[8]. Ionospheric irregularities inducing scintillations on L-band signals are due to different causes depending on the latitude. In particular, at high latitude, scintillations are mainly caused by the solar wind-magnetosphere-ionosphere coupling (see e.g. [9]), while at low latitude (where they are more likely to occur) are mainly due to the formation of small

scale irregularities embedded in the Equatorial Plasma Bubbles (EPB) (see e.g. [10]–[14]). At mid latitude, ionospheric scintillations can be due to poleward expansion of the crests of the Equatorial Ionization Anomaly (EIA) [15] or equatorward expansion of the auroral oval during geomagnetic storms [16]. Very few cases of mid latitude GNSS scintillations during quiet times are reported in the literature [17]. By exploiting the GNSS signals transmitted by Medium-Earth Orbit (MEO) and Geostationary-Earth Orbit (GEO) satellites as signals-of-opportunity, it is possible to investigate the ionospheric irregularities for scientific purposes, as well as to monitor ionospheric scintillations in the framework of operational space weather services [18]. This is achieved by means of ground-based passive instruments, such as the GNSS Ionospheric Scintillation and TEC Monitor (GISTM) receivers [19] which provide the estimation of the so-called amplitude and phase scintillation indices (S_4 and σ_ϕ respectively), allowing to quantify ionospheric scintillations [20]. Besides ionospheric irregularities, however, a numbers of different phenomena related to both space weather events (e.g. Solar Radio Burst [21], [22]) and environmental conditions, may impair the GNSS signals and the detection of ionospheric scintillations. A well-recognized source of error in the computation of the scintillation indices is the reception of GNSS signals from multiple paths due to the reflections caused by obstacles in the proximity of the receiving antenna, known as multipath [23]. To compensate for such phenomena, GISTM receiver antennas are typically deployed in multipath-free conditions, i.e., isolated areas with limited natural or anthropogenic obstacles, and elevation masks can be configured to neglect multipath-susceptible signals received from low-elevation satellites [24].

Similarly to the multipath, misleading effects on navigation signals and the derived scintillation indices can also be observed due to intentional or unintentional in-band Radio Frequency Interference (RFI)s, captured by instruments' receiving antennas [23], [25]–[27]. These interferences are typically attributed to malicious actions aiming at disrupting GNSS receivers' operational activities by forcing misleading Position, Velocity, Timing (PVT) estimation, degrading their estimation accuracy up to cause a denial of their Positioning, Navigation and Timing (PNT) capabilities (a.k.a. Denial-of-Service (DoS) attack) [28]. These attacks are classified as spoofing, meaconing, and jamming, with the first aiming at fooling receivers' operations by transmitting plausible yet structured or unstructured Radio Frequency (RF) signals to

E. Pica and C. Cesaroni are with the Environment Department of the Istituto Nazionale di Geofisica e Vulcanologia (INGV), Rome (Italy)

A. Minetto and F. Dovis are with the Department of Electronics and Telecommunications (DET), Politecnico di Torino, Turin (Italy), e-mail: name.surname@polito.it.

Manuscript received MONTH XX, XXXX; revised MONTH XX, XXXX.

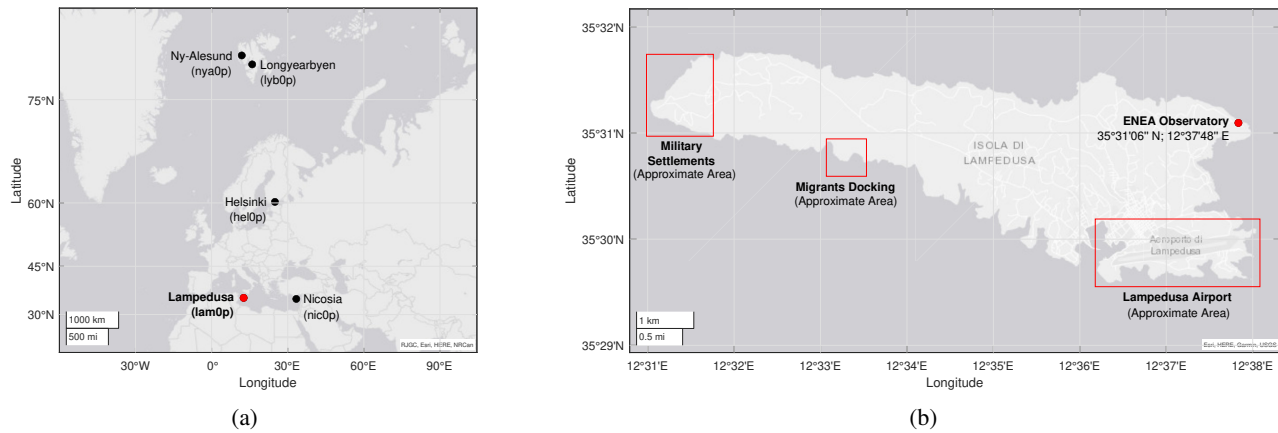


Fig. 1: INGV ionospheric scintillation monitoring network in the European area (Fig. 1a) and detail of Lampedusa island (Italy) showing the position of the ENEA observatory and other areas of interest (Fig. 1b).

90 disturb or blind the receiver's RF chain. Despite a lack of
 91 literature, alternative yet unauthorized misuse of the GNSS
 92 bands may be also referred to as RF steganography [29], [30],
 93 aiming at hiding data transmission in unsuspected portions
 94 of the RF spectrum. Such undocumented actions may turn
 95 into GNSS jamming when the received RFI power is at least
 96 comparable to the received power of legitimate GNSS signals.
 97 Despite the effects of RFIs on the PNT performance of GNSS
 98 receivers can be quantified through systematic analysis [31],
 99 the impact of RFIs on the computation of the scintillation
 100 indices have been only demonstrated through a controlled
 101 simulation environment in few pioneering studies [25], [26].
 102 In order to detect RFIs in real scenarios, Intermediate Fre-
 103 quency (IF) or baseband samples of GNSS signals can be
 104 recorded and analyzed by emulating the processing chain of a
 105 conventional GNSS receiver through highly-flexible Software
 106 Defined Radio (SDR) framework [32], [33]. To this aim, the
 107 use of SDR equipment has been demonstrated as a powerful
 108 tool to support the analysis of GNSS signals recorded at
 109 remote locations [34], [35]. Further examples of RFI detection
 110 strategies are extensively documented in satellite-based remote
 111 sensing applications that leverage similar approaches [36]–
 112 [39].

113 In this article we present the investigation carried out by the
 114 Istituto Nazionale di Geofisica e Vulcanologia (INGV) and the
 115 Department of Electronics and Telecommunications (DET) of
 116 Politecnico di Torino to assess the nature of several anomalies
 117 observed in the S_4 index computed by a GISTM receiver oper-
 118 ating in Lampedusa island (35°31'06" N; 12°37'48" E), Italy.
 119 The observatory is part of the ING V ionospheric monitoring
 120 network [40] shown in Fig. 1a and is hosted at the Climate
 121 Observation Station of the Italian National Agency for New
 122 Technologies, Energy and Sustainable Economic Development
 123 (ENEA), visible in Fig. 1b. At the mid-latitudes monitored
 124 by the receiver, the aforementioned anomalies were observed
 125 for the first time during summer 2020, but similar seasonal
 126 repetition and daily patterns appears again during 2021. Unlike
 127 low-latitudes, ionospheric scintillations in the Mediterranean
 128 sector do not show any seasonal or daily regular patterns and
 129 are due, as already pointed-out, to disturbed geomagnetic con-

130 ditions. Moreover, the political and environmental situation of
 131 Lampedusa may favor deliberate RF transmissions against nav-
 132 igation and communication systems: the island hosts military
 133 settlements and NATO radar equipment, a civilian and military
 134 airport, and is a hotspot of irregular migratory flows from the
 135 coast of North Africa [41], [42]. Furthermore, possible RFIs
 136 in the area were detected in the second semester of 2020 by
 137 Airbus aircrafts [43] and a recent paper has highlighted intense
 138 RFIs in the Mediterranean region by analyzing the data of the
 139 GNSS receivers carried by GRACE Follow-On (GRACE-FO)
 140 Low Earth Orbit (LEO) satellites [44].
 141 Moving from the know-how gathered during previous, joint
 142 test campaigns and activities [34], [45], [46], a renewed, SDR-
 143 based hardware and software architecture was designed and
 144 implemented to perform long-term grabbing of GNSS RF
 145 signal samples in the attempt to identify and characterize the
 146 source of the disturbances.

147 The main contributions of the article are the following:

- 148 • we prove the presence of an interferer affecting the GNSS
 149 signal in the Lampedusa area and present a characteriza-
 150 tion of the RFI through the analysis of the IF samples
 151 acquired by the dedicated SDR architecture. We discuss
 152 the impact of such interference on the estimation of
 153 the amplitude scintillation index and propose an analytic
 154 model of the interferer, which may allow for further
 155 theoretical analyses and the development of mitigation
 156 techniques.
- 157 • we assess the adverse impact of the RFIs on the scintil-
 158 lation data computed through the GISTM receiver, which
 159 may impair both near real-time monitoring applications
 160 as well as scientific investigations of ionospheric scin-
 161 tillation. At the time of writing, on-field proofs of such
 162 a vulnerability are still undocumented in the literature.
 163 We also propose a preliminary methodology to automati-
 164 cally detect and filter the interfered observation from the
 165 collected data.

166 The article is organized as follows: Section II provides
 167 background information about the computation of scintillation
 168 indices through GNSS signals in GISTM receivers. Section III
 169 presents a preliminary analysis of the anomalies detected in the

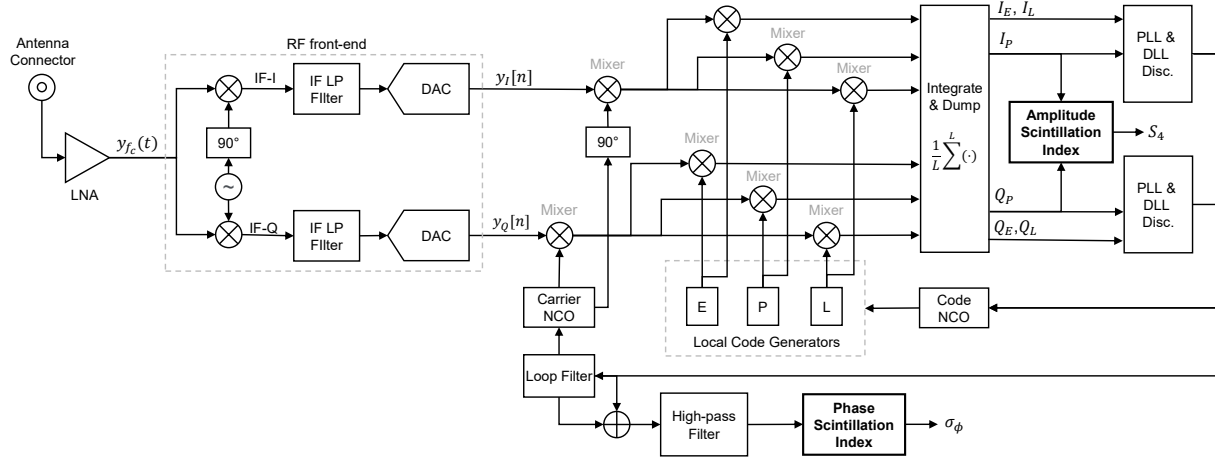


Fig. 2: Block diagram of a conventional, single-channel tracking loop architecture for GNSS receivers. I_p and Q_p outputs from the prompt correlator (P) are employed in the estimation of amplitude scintillation indices, i.e. S_4 , while σ_ϕ is estimated through the output of the loop filter in charge of tracking the IF or the residual carrier frequency.

scintillation data generated by the GISTM receiver, with the aim to eventually exclude real scintillation phenomena induced by the ionosphere as the cause of the observed anomalies. Section IV describes the experimental SDR setup deployed at the monitoring station and presents the analysis tools exploited for the investigation and characterization of the interferer as well as for the detection and filtering of the anomalies from the scintillation data. Section V reports the results of the aforementioned analysis, while a discussion about the results and hypothesis about the nature of the disturbances are reported in Section VI. Conclusions and further works are eventually drawn in Section VII.

II. BACKGROUND

A. GNSS signal and receiver models

To provide ionospheric scintillation indices, a GNSS receiver must receive GNSS signals from Line-of-Sight (LOS) satellites and track their numerical counterparts. Signals from multiple satellites are managed in a multi-channel architecture, and the associated indices are independently provided for each channel. According to the scheme of Fig. 2, the received signal at the input of the receiver's front-end is modelled as

$$y_{f_c}(t) = x_{\text{GNSS},f_c}(t) + x_{\text{RFI}}(t) + w_{\text{RX}}(t) \quad (1)$$

where x_{GNSS,f_c} is the sum of the received GNSS signals from the visible satellites at the receiver location for a given bandwidth and center frequency f_c [47], and x_{RFI} identifies any possible incoherent, in-band RFI [28]. Both useful and interfering signal components in (1) account for non-idealities due to the respective RF propagation channels. Eventually, w_{RX} models the additive thermal noise introduced by the receiving chain and the quantization noise injected by the Analog-to-Digital Conversion (ADC) operated at the RF front-end. Within this study, GNSS signals are considered continuously available at the receiver while RFI terms may occasionally occur. The RF front-end downconverts the input signal to a pre-defined IF prior to its sampling and quantization

at the ADC. As shown in Fig. 2 the baseband numerical samples from In-Phase (I) and Quadrature (Q) branches are correlated with early (E), prompt (L) and late (L) replicas of the locally-generated spreading code. Eventually, the Integrate & Dump block provides prompt In-Phase (I_p) and Quadrature (Q_p) samples which are used to estimate the S_4 index, while the σ_ϕ index is derived through the output of the loop filter in charge of tracking the IF carrier, as depicted by the bottom branch of the diagram in Fig. 2.

B. Amplitude and phase scintillation indices

The S_4 and σ_ϕ are the statistical indices typically adopted to quantify ionospheric scintillations based upon received GNSS signals features. S_4 measures the variability of the signal intensity (SI), that is estimated as

$$SI = WBP - NBP \quad (2)$$

where Wide-Band Power (WBP) and Narrow-Band Power (NBP) are respectively defined as

$$WBP = \sum_{i=0}^M (I_i^2 + Q_i^2) \quad (3)$$

and

$$NBP = \left(\sum_{i=0}^M I_i \right)^2 + \left(\sum_{i=0}^M Q_i \right)^2 \quad (4)$$

and the I and Q terms in (3) and (4) are the I_p and Q_p components of the received signal after the integrate and dump operation performed by the receiver tracking stage and M is the total number of accumulated periods. The S_4 index is defined as the normalized standard deviation of the detrended 50 Hz raw signal intensity over a given interval of time, typically 60 s

$$S_4' = \sqrt{\frac{\langle SI^2 \rangle - \langle SI \rangle^2}{\langle SI \rangle^2}} \quad (5)$$

TABLE I: Conventional thresholds for the classification of ionospheric scintillation events based upon amplitude and phase indices [49].

Index	Event Intensity	Threshold
S_4	Quiet	$S_4 \leq 0.1$
	Weak	$0.1 < S_4 \leq 0.25$
	Moderate	$0.25 < S_4 \leq 0.7$
	Severe	$S_4 > 0.7$
σ_ϕ (rad)	Quiet	$\sigma_\phi \leq 0.1$
	Weak	$0.1 < \sigma_\phi \leq 0.25$
	Moderate	$0.25 < \sigma_\phi \leq 0.7$
	Severe	$\sigma_\phi > 0.7$

where $\langle \cdot \rangle$ is the time average operator over the observation window. The contribution of the noise to the overall value of S_4 can be estimated as

$$S_{4,n} = \sqrt{\frac{\alpha}{\langle C/N_0 \rangle} \left(1 + \frac{\beta}{\gamma \langle C/N_0 \rangle} \right)} \quad (6)$$

where C/N_0 is the estimated carrier-to-noise ratio [48], and $\alpha = 100$, $\beta = 500$, $\gamma = 19$, as proposed in [20]. Equation (6) provides an estimate of the noise standard deviation over the target timespan (i.e., 60s) and is typically obtained through the signal component, I or Q , carrying a nearly-orthogonal spreading code which does not correlate with the code of interest, thus returning a noise-like behavior. Eventually, a refined estimate of S_4 can be computed by removing the noise contribution, as

$$S_4 = \sqrt{(S'_{4,n})^2 - S_{4,n}^2} \quad (7)$$

The estimation of S_4 through (7) may be affected by unexpected variation of the C/N_0 unrelated to ionospheric irregularities, such as in presence of RFIs producing misleading values of the index thus triggering false evaluation of amplitude ionospheric scintillation.

The σ_ϕ index is defined as the standard deviation of the 50 Hz detrended carrier phase over a given interval of time, typically 60 s and is given in radians, as

$$\sigma_\phi = \sqrt{\langle \Phi^2 \rangle - \langle \Phi \rangle^2} \quad (8)$$

The σ_ϕ seems not affected by the events investigated in this study but it will be recalled for the sake of completeness in Section III for an exhaustive analysis of the anomalous scintillation events. The scintillation indices are calculated along the line-of-sight (slant S_4 and σ_ϕ) of the GNSS signals transmitted by those satellites in the receiver's Field of View (FoV) and filters with a fixed cutoff frequency of 0.1 Hz are usually adopted for data detrending. The detection of ionospheric scintillations can be performed by comparing the aforementioned indices against predefined thresholds, allowing a preliminary classification of the severity of the events; typical thresholds and associated events intensity are reported in Table I.

III. PRELIMINARY ANALYSIS

A. Lampedusa GISTM station

The ionospheric observatory of Lampedusa hosts, since 2018, a Septentrio PolaRx5S GISTM receiver. The PolaRx5S is a multi-frequency, multi-constellation GNSS receiver equipped with a low-noise Oven Controlled Crystal (Xtal) Oscillator (OCXO). It acquires, for every satellite in view and for every available frequency, the raw phase (in cycles) and post-correlation I_p and Q_p samples with a sampling rate of 50 Hz, as per the generalized architecture presented in Section II-A. It is able to provide, with a 1-minute resolution, the S_4 and σ_ϕ indices together with the Total Electron Content (TEC) and its Rate of Change (ROT). The data acquired by the station are transmitted in near-real time to the INGV-SWIT (Space Weather Information Technology) system and collected into a database publicly accessible to the scientific community through the eSWua (electronic Space Weather upper atmosphere: eswua.ingv.it) website [50]. These data are also provided to the PECASUS consortium (www.pecasus.eu) for the provision of Space Weather services to the International Civil Aviation Organization (ICAO) [18].

B. Investigation about the S_4 anomalies

The following analysis focuses on the scintillation indices recorded by the GISTM receiver during August 2021 wherein several anomalies were observed in the collected data. In order to avoid misleading contributions possibly caused by multipath-effects, only satellites with elevation above 30° are considered; indeed, the Lampedusa observatory is located nearby a lighthouse, whose building was proven as a non-negligible source of multipath for those signals acquired at lower elevations, as it will be shown in the results of Section V-C. The area observed by the receiver, considering this elevation mask, cover the mid-latitudes between 30°N and 40°N and a longitudinal sector between 7°E and 19°E . The signals taken into consideration are the one belonging to the Global Positioning System (GPS), Galileo, BeiDou Navigation Satellite System (BDS) and GLONASS constellations. The reported S_4 and σ_ϕ indices are the slant values calculated at 1-minute resolution from the L1/E1 frequency band for each satellites in view in the considered timespan.

Fig. 3a and Fig. 3b reports the maximum hourly values of the S_4 and σ_ϕ respectively, recorded during August 2021. As it is possible to see from Fig. 3a, several occurrences of the S_4 above the threshold of moderate scintillation (lower dotted red line in Fig. 3a and Fig. 3b) recurred during the month; the same behavior was not registered for the σ_ϕ (Fig. 3b).

The observed values of the S_4 are definitely unexpected considering i) the latitudes covered by this analysis and ii) the overall space weather conditions registered during the month of August 2021. Indeed, as mentioned in Section I, ionospheric scintillation at the Mediterranean latitudes are not common and are generally caused by disturbed space weather conditions [15], [16], [51], [52] originating the so-called super fountain effect [53]. However, as Fig. 3c shows, no relevant geomagnetic storms capable to induce a poleward expansion of the crests of the EIA were detected during August

2021 according to the local K-index recorded at the INGV
 Geomagnetic Observatory of Lampedusa [54], [55]. It is worth
 recalling that the K-index quantifies the disturbances in the
 horizontal component of the magnetic field with respect to
 the quiet conditions and can be employed as an indicator
 of the intensity of geomagnetic storms measured at a given
 geomagnetic observatory [56]. Usually, K-index values below
 4 are representative of quiet/low-disturbed conditions, while
 values from 5 to 9 indicate minor to extreme storm condi-
 tions, respectively. Moreover, the diffractive effects induced by
 ionospheric irregularities on the GNSS signals passing through
 them will produce fluctuations of both the phase and amplitude
 of the signals, thus increasing the value of both the S_4 and
 σ_ϕ indices [5], [57], contrary to what shown by Fig. 3a and
 Fig. 3b.

Further considerations on the observed temporal and spatial
 distribution of the scintillation indices, when compared to
 the case of a real ionospheric scintillation event, allow to
 eventually exclude ionospheric phenomena as the source of
 the observed anomalies. The following analysis focuses on
 the data of the 7th August 2021, when several anomalies
 were recorded, compared to the data of the 10th March
 2022, when a real ionospheric scintillation event was detected
 over the area under investigation. With regards to the data
 of the 7th of August 2021, Fig. 4a reports a daily view of
 the time profiles of the S_4 index, where different colors are
 attributed to the different satellites in view (Space Vehicle ID
 are reported in the legend). As Fig. 4a shows, the occurrences
 above the threshold of moderate scintillation seems to affect
 the signals from the majority of the satellites in view during
 the day; on the contrary, the time profile of the σ_ϕ does not
 exhibit similar patterns, as shown by Fig. 4b. Fig. 4c reports
 a daily view of the maximum (blue line) and mean (green line)
 values of the S_4 index calculated on all the signals in
 view. As Fig. 4c suggests, most of the satellites in the FoV
 exhibit similar patterns; as a consequence, the S_4 mean and
 maximum values appears to be very close each other. Fig. 4d
 shows a daily view of the time profiles of the maximum S_4
 values calculated among all the signals pertaining the same
 satellites constellation. From Fig. 4d, it is possible to spot
 similar patterns among the GPS (blue line), Galileo (red line)
 and BDS (yellow line) satellites, while GLONASS satellites
 (purple line) seems to be not affected by scintillations most
 of the time. Finally, Fig. 6a reports on a geographic map the
 S_4 occurrences above the threshold of moderate scintillation
 ($S_4 > 0.25$) during the same day (7th August). The points
 on the map represent the Ionospheric Pierce Points (IPP)s
 at 350 km for all the satellites in view and their color
 represents the values of the S_4 . As Fig. 6a shows, moderate
 to severe scintillations are visible across the entire FoV of the
 receiver, while ionospheric scintillations in quiet geomagnetic
 conditions are more likely to occur in the proximity of the EIA
 crests, respectively at ca. $\pm 20^\circ$ from the magnetic equator.
 Similar features of the spatial and temporal distributions of
 the scintillation indices reported for the 7th of August were
 eventually observed in each day of August 2021 affected by
 the anomalies.

When comparing the previous temporal and spatial distri-

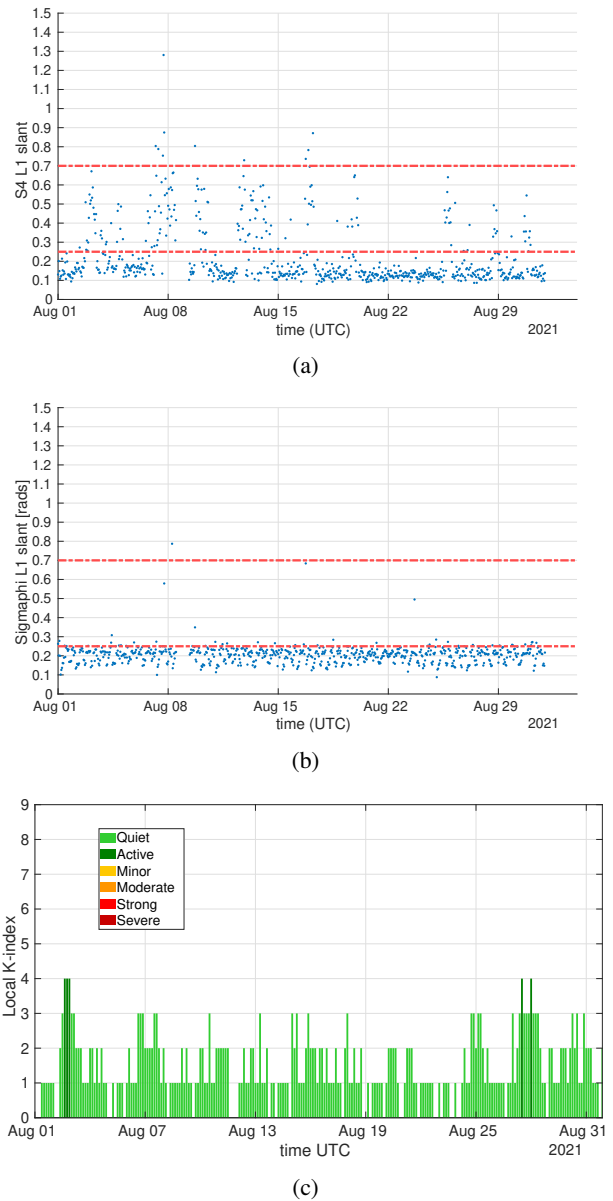
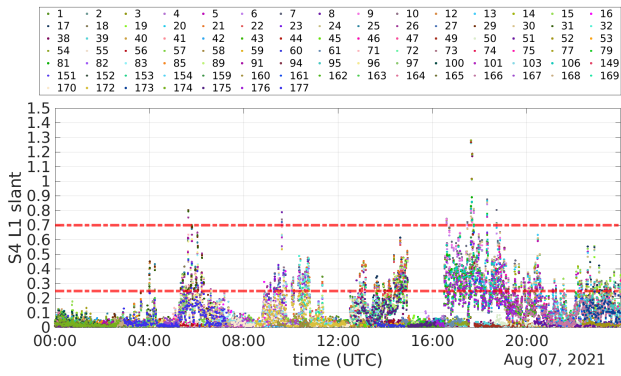
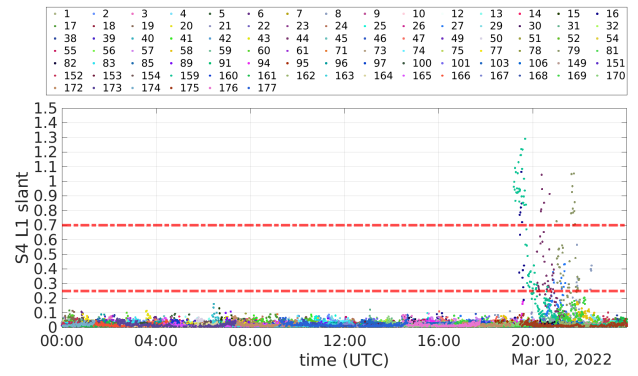


Fig. 3: Maximum hourly values of the S_4 (Fig. 3a) and σ_ϕ (Fig. 3b) indices during August 2021 (satellites elevation above 30°) and local K-index (Fig. 3c) recorded during the same period. Thresholds (dashed horizontal lines) of Fig. 3a and 3b are defined according to Table I.

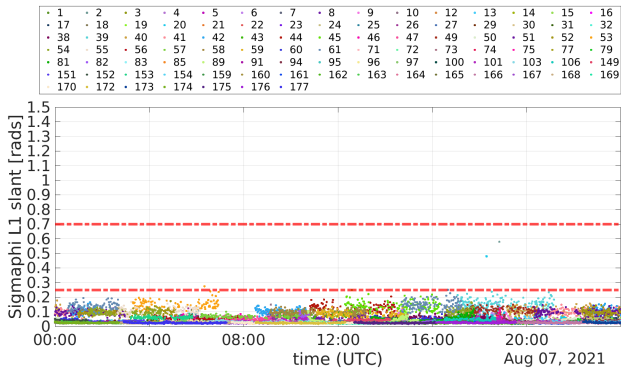
butions of the indices with those recorded during the event
 of the 10th of March 2022, it is possible to observe the
 expected behavior in the case of a real ionospheric scintillation
 event (images of Fig. 5 and Fig. 6b) and eventually conclude
 that the anomalies were not induced by natural ionospheric
 phenomena. Indeed, given the small scale (a few hundreds of
 meters) of the irregularities leading to L-band scintillations,
 and considering the latitudes under investigation, not all the
 satellites in the FoV of the receiver are expected to be affected
 by scintillations; as a consequence, the mean and maximum
 values of the S_4 will exhibit different patterns, as shown by
 Fig. 5c (contrary to Fig. 4c, when the RFI was present), and



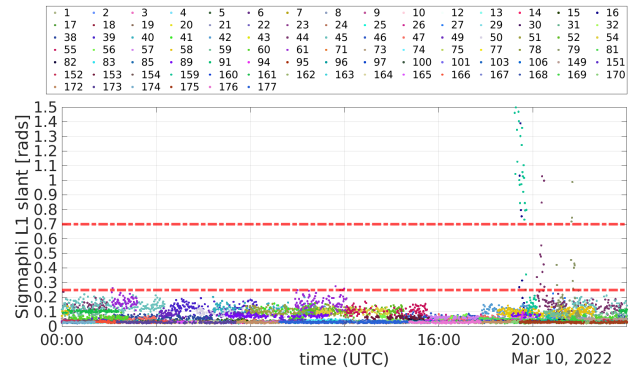
(a) Time profile of the S_4 . Different colors are attributed to the different satellites in view (Space Vehicle ID in the legend).



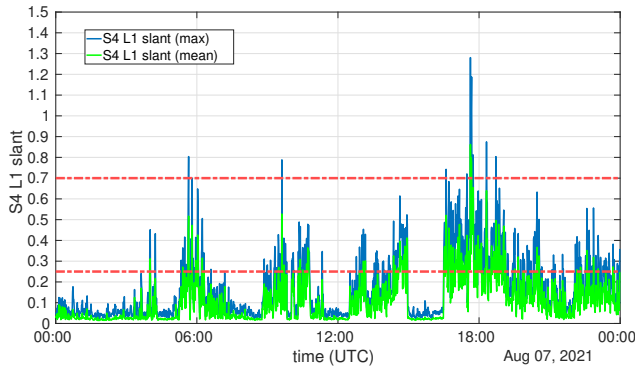
(a) Time profile of the S_4 . Different colors are attributed to the different satellites in view (Space Vehicle ID in the legend).



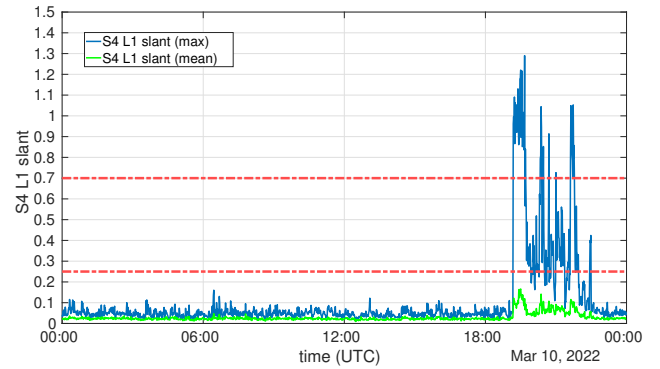
(b) Time profile of the σ_ϕ . Different colors are attributed to the different satellites in view (Space Vehicle ID in the legend).



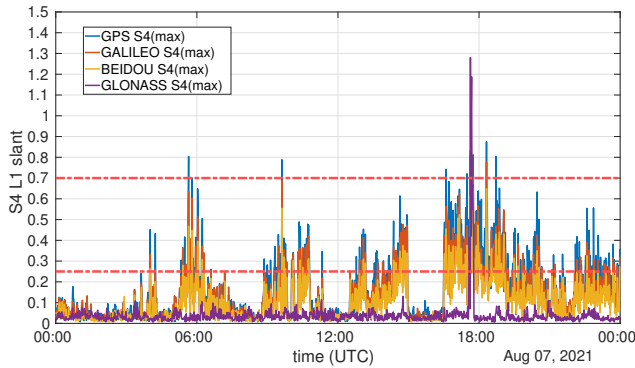
(b) Time profile of the σ_ϕ . Different colors are attributed to the different satellites in view (Space Vehicle ID in the legend).



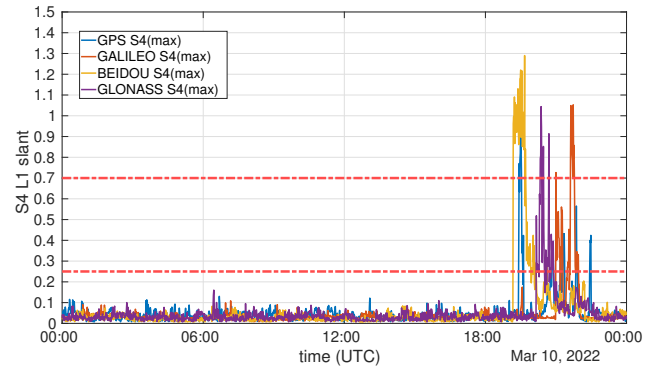
(c) Time profile of the S_4 by considering maximum and mean values among all the available satellites.



(c) Time profile of the S_4 by considering maximum and mean values among all the available satellites.



(d) Time profile of the S_4 by considering the maximum values among all the satellites pertaining the same GNSS constellation.



(d) Time profile of the S_4 by considering the maximum values among all the satellites pertaining the same GNSS constellation.

Fig. 4: (7th of August 2021) Scintillation indices affected by RFI. Thresholds (dashed horizontal lines) are defined according to Table I.

Fig. 5: (10th of March 2022) Scintillation indices in case of real ionospheric scintillation event. Thresholds (dashed horizontal lines) are defined according to Table I

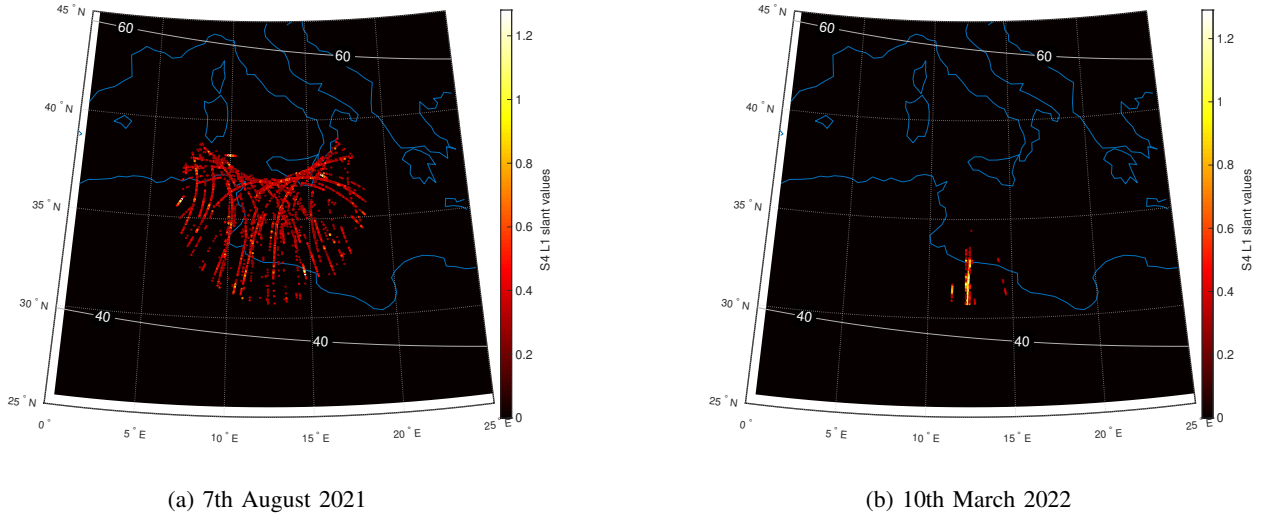


Fig. 6: Map of the S_4 occurrences above the threshold of moderate scintillation ($S_4 > 0.25$) for the 7th of August 2021 (Fig. 6a) and for the 10th of March 2022 (Fig. 6b) and for satellites elevation above 30° . Geographic coordinates are labeled at the border of the maps and represented by the dotted lines inside the map; geomagnetic latitudes are labeled inside the maps and represented with the continuous lines.

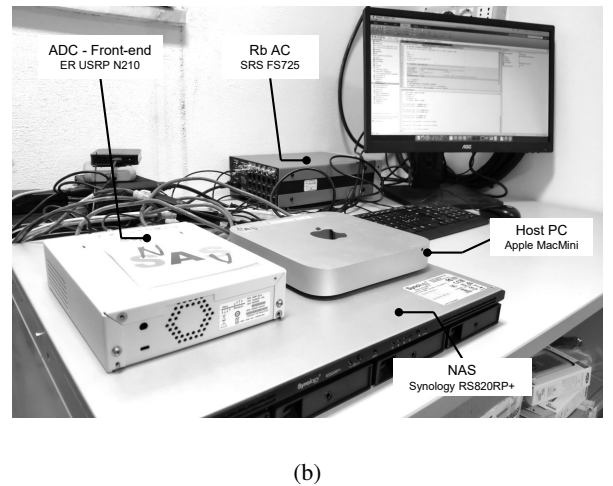
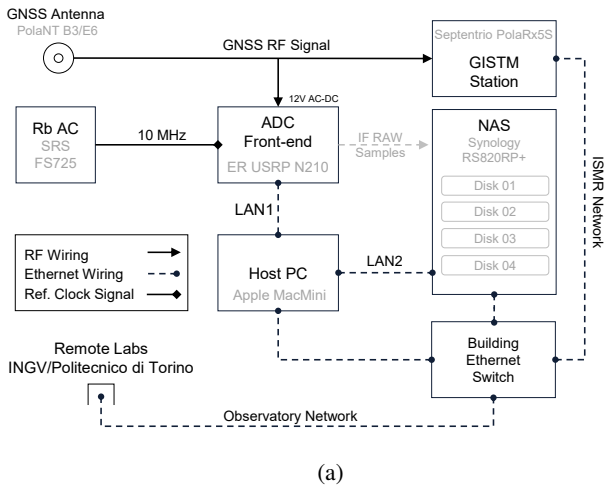


Fig. 7: Operational GISTM/SDR architecture for the grabbing of GNSS IF signal samples (Fig. 7a), and actual deployment of the GISTM/SDR set-up along with complementary equipment at the ENEA Station for Climate Observations in Lampedusa (Fig. 7b).

387 only localized area will result affected by scintillation, as
 388 shown by Fig. 6b (contrary to what is shown by Fig. 6a).
 389 Moreover, ionospheric irregularities will impact the signals of
 390 any GNSS Constellation passing through them, as shown by
 391 Fig. 5d (in comparison to Fig. 4d), and will induce scintillation
 392 on both amplitude and phase of the signals, as shown by
 393 Fig. 5a and Fig. 5b (in comparison to Fig. 4a and Fig. 4b,
 394 respectively).

IV. METHODOLOGY

A. Experimental Setup and data collection

395
 396 In September 2021, new investigations were carried-out to
 397 assess the nature of the anomalies presented in Section III.
 398

399 In order to acquire possibly-interfered GNSS signals, a dedi-
 400 cated experimental setup was deployed alongside the GISTM
 401 receiver, based on a SDR architecture. A high-level block
 402 scheme of the setup is provided in Fig. 7a while a picture
 403 of the operational hardware deployment is shown in Fig. 7b.
 404 General-purpose SDR front-ends are typically employed for
 405 research and development activities in radio-communication
 406 systems as they facilitate the acquisition of RF signals through
 407 configurable and flexible hardware and software architectures.
 408 By exploiting such flexibility, the setup aims at collecting
 409 IF signals samples of the received GNSS L1-band (center
 410 frequency 1575.42 MHz) to perform investigations on possible
 411 intentional or unintentional interferences affecting the GNSS
 412 signals (and the derived scientific data) recorded on the island.

TABLE II: Configuration parameters of the front-end and the acquisition software.

Symbol	Definition	Value
f_0	Center frequency	1575.42 MHz (L1)
f_{IF}	Intermediate frequency	0.00 MHz (baseband)
f_s	Sampling frequency	5 Msps
b_d	Bit depth	16 bit (8I+8Q)
ΔT	acquisition interval	600 s (10 minutes)
T_{S_4}	S_4 Threshold	0.3

At the time of writing, the experimental setup consists of an Ettus Research™ Universal Software Radio Peripheral (USRP) N210 front-end performing the ADC conversion of the input signal, and the grabbing of IF signal samples; an Apple MacMini PC, i.e., the host PC, that runs the signal acquisition routine; a Stanford Research Systems (SRS) Rubidium (Rb) Atomic Clock (AC) FS725 to provide stable and reliable 10 MHz reference signal to the ER USRP, and a Network-Attached Storage (NAS) for the storage of large data volume. A 2-way splitter is exploited to feed both the GISTM receiver and the front-end with the RF signals received at the GNSS PolaNt Choke Ring B3/E6 antenna. The acquisition routine, continuously executed on the host PC, is being part of a proprietary GNSS fully-software receiver designed to emulate the processing chain of commercial receivers in a more flexible and controllable environment. The configuration parameters of the front-end and of the aforementioned acquisition routine are reported in Table II. To partially overcome the well-known issue of storing TBs of binary files produced by such systems, the Lampedusa setup took advantage of a NAS unit which directly stores the IF signal samples during the acquisition. Moreover, a fully-automated procedure continuously acquires 24/7 the IF samples and daily freed the space on the NAS from the non-useful datasets.

The first collection campaign provides 171 datasets of 10 minutes each (28.5 hours), affected by the RFI with different intensity and time behavior. The collected datasets is included in an open data collection, i.e., Lampedusa Scintillation Monitoring Interfered Data (LAMP_SMID_2109)¹, and an overview of their time distribution over the test campaign is shown in Table III.

B. Post-processing Signal Analysis (SDR data)

The binary files recorded at the station during the acquisition campaign were analyzed in post-processing via a dedicated MATLAB framework. The proposed analysis was pursued to investigate the nature of the interferer and provide a preliminary characterization of the signal, as well as a quantification of its effect on the estimation of the S_4 .

1) *Spectral analysis through Power Spectral Density (PSD) estimation*: the analysis was performed through a PSD estimator, i.e., Welch spectrogram [58], [59], on signal snapshots

with a duration of 1 s, and on the full capture of 10 minutes, according to

$$P_y(f) = \frac{1}{M} |\text{FFT}[y[n]]|^2 \triangleq \frac{1}{M} \left| \sum_{n=0}^{N-1} y[n] e^{j2\pi nk} \right|^2 \quad (9)$$

where M is the amount of signal samples and N is the amount of evaluation point of the Fast Fourier Transform (FFT). The Welch PSD is hence given by averaging the periodogram as

$$S_y^W(f) \triangleq \frac{1}{K} \sum_{m=0}^{K-1} P_y(f) \quad (10)$$

where K is the amount of frames over which the power spectrum is averaged and W identifies the Welch formulation [58]. The analysis provided a preliminary feedback on possible spectral anomalies with respect to GNSS signals observed in nominal conditions.

2) *Persistence Spectrum*: was adopted to investigate the RFI spectral signature and the stability of an intelligible PSD over short time periods [60]. This analysis is based on the accumulation of Welch spectrograms (9) on a grided PSD plot. The longer a particular PSD envelope persists in a signal as the signal evolves, the higher its time percentage and thus the brighter is the heatmap in the plot. The tool is also helpful to identify hidden coherent signals in noisy patterns as well as sporadic or fast pulsed signals with unknown duty cycles.

3) *Time-Decimated Time-Frequency Analysis (TD-TFA)*: was performed through the estimation of partially-overlapping Short Time Fourier Transform (STFT). A signal chunk composed by N samples is filtered through a shaped window of length K , and a Discrete Fourier Transform (DFT) is computed over N_{DFT} points. The window slides over the next N samples with an overlap of the previous L samples, and a DFT is performed for each window. By sliding the window along the samples vector, a Time-Frequency Analysis (TFA) provides a time-frequency view showing the evolution of the frequency content of a signal along the time [61]. The technique was exploited to describe the evolution of the signal by measuring its PSD profile over the whole acquisition time-span. To reduce the size of the output data, a time decimation (TD) was performed by skipping a pre-defined timespan in between subsequent signal chunks, with an acceptable reduction of the time resolution. Shorter signal time spans are preferable in terms of time consumption since they allow faster STFT computation, by dealing with smaller amounts of samples. In terms of readability of the TD-TFA output figures, the following options provided similar results

- A. $t_i = 20$ ms and $t_s = 100$ ms \rightarrow 285 MB
- B. $t_i = 1$ s and $t_s = 1$ s \rightarrow 28.5 MB

where t_i is the integration interval and corresponds to the overall duration of the signal samples processed through STFT, and t_s is the skip interval included between two subsequent integration intervals. While the first corresponds to the actual amount of input data, the latter indicates the duration of unprocessed signal chunks, thus representing the decimation factor of the proposed TD-TFA. TFA analysis contains more information in configuration A, however, this appeared not relevant as it does not significantly impact the visual detection

¹<http://iecc-dataport.org/10996>

TABLE III: Amount of datasets collected during the September test campaign in Lampedusa, and available in the LAMP_SMID_2109 open data collection.

Date	Hour of the day (UTC)																							
	00	01	02	03	04	05	06	07	08	09	10	11	12	13	14	15	16	17	18	19	20	21	22	23
16-Sep-2021																				6				
17-Sep-2021	1 ^a			6	6									6	6	6	6	6				5	6	5
18-Sep-2021	6	6		6	6	6	6													6	6	6	6	6
19-Sep-2021	6	6	5	6		5																		
27-Sep-2021																				6				6

^aReference dataset not automatically retrieved by the system but still affected by low-intensity RFI.

of the interference signature in both time and frequency domains. Therefore, a suitable trade-off between frequency, time resolutions and storage occupancy of the TD-TFA output results was provided through the configuration B.

4) *GNSS signal tracking*: it was performed on the acquired datasets to quantify the impact of the RFI on GNSS receivers tracking stage, thus assessing the induced jamming effect on navigation signals in terms of C/N_0 . The signal tracking leverages the cross-correlation of Direct-Sequence Spread Spectrum (DSSS) Code Division Multiple Access (CDMA) signals transmitted by GPS and Galileo satellites. The software receiver architecture imitates the conventional channel tracking already described in Fig. 2. For the scope of these analysis, the tracking was performed on the acquired GNSS signals with a coherent integration time $T_c = 0.020$ s. A key metric for the conditioning of S_4 is the C/N_0 measured at each channel. According to the analysis presented in Section III, common effects are expected to be concurrently observed on different satellites signals. Therefore, we propose an aggregate estimation of the variation of C/N_0 , namely $\delta C/N_0$, with respect to the mean value used in (7). Formally, an estimate of the C/N_0 is given by

$$C/N_0 = 10 \log_{10} (\text{SNR} B_{eq}) \quad (11)$$

where $B_{eq} = 1/T_c$ with T_c stands for the coherent integration time, and

$$\text{SNR} = \frac{1}{2M} \sum_{i=0}^M \frac{(|I_i| - |Q_i|)^2}{I_i^2 + Q_i^2}. \quad (12)$$

The C/N_0 is hence computed over a window of length M that is typically set to $1/T_c$. To be consistent with the definition of the indices provided in Section II-B, its aggregated variation for all the tracked signals has to be measured by averaging the 60 s de-trended series of the respective C/N_0 (11), as

$$\delta C/N_0 = \frac{1}{S} \sum_{j=0}^S \left((C/N_0)_W^{(j)} - \langle (C/N_0)_W^{(j)} \rangle \right) \quad (13)$$

where j refers to the j -th GNSS signal, $W = 60$ s indicates the observation window, and S refers to the overall number of available signals.

5) *RFI signal emulation and model*: provided the features observed through the above-mentioned analysis tools and the recent literature on GNSS interferences and threats, a signal with similar features was numerically simulated and reproduced by means of a MATLAB routine.

C. Analysis of the GISTM scintillation data

1) *Ground Based Scintillation Climatology (GBSC)*: It consists in building maps of the percentage occurrences of the scintillation indices above a predefined threshold and evaluated over a certain time period [2]. The climatological maps report the percentage occurrences on a bi-dimensional time-grid having the hour of the day in the horizontal axis and the day of the year in the vertical one or as geographic maps, showing the percentage occurrences evaluated over geographic cells with a given spatial resolution. The technique is used to perform climatological analysis of scintillation events, but it can also be adopted to highlight the spatial and temporal features of scintillations over shorter time-periods (e.g. few months). With regards to the S_4 index, the S_4 percentage occurrences in a given time-interval (S_{4POt}) is evaluated as:

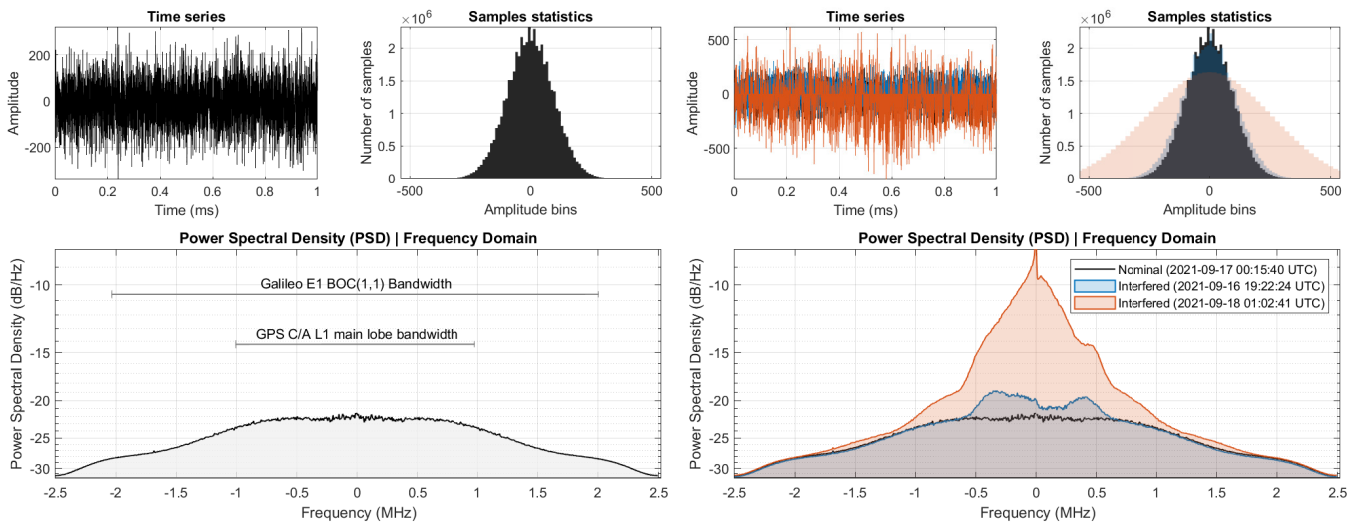
$$S_{4POt} = \frac{S_{4thr}(\Delta t)}{S_{4tot}(\Delta t)} \quad (14)$$

where $S_{4thr}(\Delta t)$ is the total number of the S_4 occurrences above the chosen threshold in the given time-interval Δt and $S_{4tot}(\Delta t)$ is the overall number of S_4 measurements available in the same time-interval. The S_4 percentage occurrences over a specific geographic cell (S_{4POs}) is evaluated as:

$$S_{4POs} = \frac{S_{4thr}(\Delta t, \Delta lat, \Delta lon)}{S_{4tot}(\Delta t, \Delta lat, \Delta lon)} \quad (15)$$

where $S_{4thr}(\Delta t, \Delta lat, \Delta lon)$ is the total number of the S_4 occurrences above the chosen threshold in the given time-interval Δt and limited to the specific geographic cell (range of latitudes Δlat and longitudes Δlon), while $S_{4tot}(\Delta t, \Delta lat, \Delta lon)$ is the overall number of S_4 measurements available in the same time-interval and pertaining the same geographic cell.

2) *RFI filtering*: In order to remove the RFI-induced anomalies from the S_4 data, all the epochs in which the mean values of the S_4 (calculated on all the available signals at that epoch) are above a certain threshold have to be filtered out from the dataset; indeed, as follows from the considerations reported in Section III-B, the RFI has the effect of increasing the S_4 values of the majority of the satellites in view at the same epoch, differently from actual ionospheric scintillation events. In the case of Lampedusa, given that the average number of satellites simultaneously in the FoV above 10° of elevation is 30, and assuming that 20 percent of the signals could be at most simultaneously affected by actual ionospheric scintillations at these latitudes, a threshold of 0.15 for the mean values of the S_4 has been chosen as a good



(a) Single dataset: signal characterization in nominal conditions (b) Multiple datasets comparison in nominal and interfered conditions

Fig. 8: Single and multiple datasets data probing performed on 1 s signal chunks by means of a GNSS signal analysis tool embedded in the GNSS software receiver.

TABLE IV: Datasets selected as representative samples of the observed anomalous GNSS signals for the presentation of the analysis results in Section V-A.

ID	Date	Start time (UTC)	End time (UTC)	$\max(S_4)$
(a)	16-Sep-2021	19:22:24	19:33:00	0.63
(b)	17-Sep-2021 ^b	00:15:40	02:26:00	0.17
(c)	18-Sep-2021	01:02:41	02:13:00	0.43
(d)	19-Sep-2021 ^b	02:20:07	02:31:00	0.18
(e)	19-Sep-2021	05:12:02	05:22:00	0.38
(f)	19-Sep-2021	05:42:22	05:52:00	0.32

^b Datasets not kept by the automated grabbing system.

583 compromise to detect most of the RFI-induced anomalies,
 584 avoiding at the same time to filtering-out possible actual
 585 ionospheric scintillation events. It has to be noted, however,
 586 that the proposed filtering technique potentially removes from
 587 the dataset the actual ionospheric scintillation events occurring
 588 contemporary the interferences.

589 V. RESULTS

590 A. Characterization of the RFI

591 This section provides a first characterization about the RFI
 592 through the analysis tools presented in Section IV-B. For the
 593 sake of conciseness, the datasets listed in Table IV have been
 594 considered as representative samples of the RFI behaviour in
 595 different conditions.

596 1) *Spectral analysis through Power Spectral Density (PSD)*
 597 *estimation:* Fig. 8a and Fig. 8b compare time series (top-left),
 598 samples histograms (top-right) and PSD (bottom) of 1 s signal
 599 snapshots belonging to three different datasets. In Fig. 8a,
 600 a dataset observed in 2021-09-17 with nominal PSD (when
 601 no interference was detected) is reported and compared in
 602 Fig. 8b with two interfered power spectra acquired during
 603 2021-09-16 and 2021-09-18. From the time series and the

604 samples histogram of Fig. 8b we observe that additional power
 605 provided by the RFI in 2021-09-16 was not significantly higher
 606 than in nominal conditions (around 3 dB); a more powerful
 607 RFI event is provided by the RFI in 2021-09-18 that visibly
 608 affect time series and histograms, and shows a more evident
 609 power density distortion in the observed bandwidth. The plot
 610 assesses the presence of a non-negligible interference lobe
 611 with a peak of about 10 dB of additional power density in
 612 the PSD (with respect to the nominal level observed in 2021-
 613 09-17). In regular conditions or under natural phenomena
 614 like ionospheric scintillations, GNSS signals are typically
 615 not affected by similar, significant variations in the observed
 616 PSD. A strong continuous wave peak appeared at the center
 617 frequency 1575.42 MHz (GNSS L1/E1 Bandwidth) and can be
 618 occasionally visible in the figures; this tone is due to a spectral
 619 leakage of the Local Oscillator (LO) operating at frequency
 620 f_c in the ER USRP N210 front-end and it does not affect nor
 621 invalidate the analysis. It has been verified that the leakage is
 622 not a component of the RFI.

623 2) *Spectral persistency and RFI spectral signature:* The
 624 set of plots in Fig. 9 shows examples of persistent spectrum
 625 analysis performed on 1 ms signal chunks every 10 s for an
 626 overall observation time of 60 s. As we can observe through
 627 the subplots, the spectral signature of the interferer consider-
 628 ably changes along the time. A nearly-symmetrical spectral
 629 signature is visible in Fig. 9d that may suggest a 2-Frequency
 630 Shift Keying (FSK) modulation. However such a signature
 631 slightly recurs only in Fig. 9b with a lower intensity, thus
 632 weakening the hypothesis. Similar asymmetrical signatures
 633 can be observed in Fig. 9a and 9e. A flattened spectral shape
 634 is instead visible in Fig. 9c and 9f where RFI intensity
 635 dramatically drops. Such a time varying behaviour makes the
 636 signal particularly difficult to be automatically identified, or
 637 tracked. Additionally, autocorrelation of time series along the
 638 observed datasets did not show any relevant similarity of the

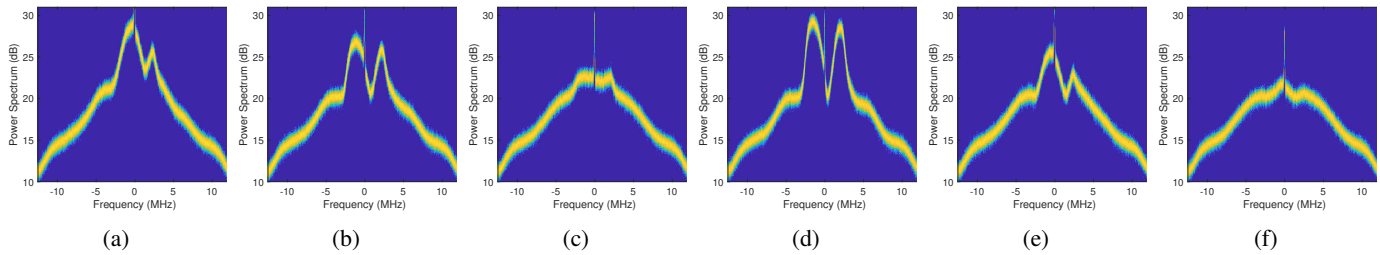


Fig. 9: Examples of persistence spectra computed on 1 ms signal chunks every 10 s to observe spectral signature stability over time. Sample dataset captured on 21-09-18 01:02:41 AM. Frequency resolution: 97.7517 kHz, time resolution: 781.28 μ s.

639 signal with itself, nor evident cyclic or recurrent components
 640 such as spreading codes or synchronization preambles. These
 641 features turn into strengths for malicious signals to not be
 642 tracked or automatically detected. In light of this, the RFI
 643 assumes the characterization of an unstructured interference.

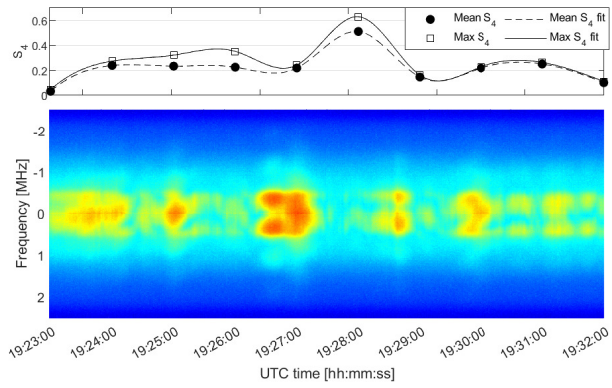
644 3) *Time-frequency analysis:* TD-TFA applied on the
 645 datasets of Table IV is shown in Fig. 10². In line with
 646 the parameters described in Section IV-B3, we set the win-
 647 dows length $K = 1 \text{ s} \cdot 10^6 \text{ Msps}$, a number of DFT points
 648 $N_{DFT} = 2^{10}$, a rectangular window of length $K = N_{DFT}$,
 649 and an overlap $L = 2^6$. As a term of comparison, the figures
 650 show in the top panels of each plot the cubic interpolation of
 651 both maximum and mean S_4 values computed by the GISTM
 652 receiver, and aligned according to the UTC time of the records.
 653 The colorscale of the PSDs is referred to the maximum
 654 observed S_4 intensity within the overall data collection (i.e.,
 655 0 dB-Hz). Frequency axis in the plots, i.e., y-axis, is centered
 656 at the target frequency, i.e. 1575.42 MHz, referred to as 0 Hz,
 657 and time scale is reported in 24-hours format. Irregular PSD
 658 behaviour is observed in time for all the collected datasets,
 659 RFI's intensity shows a remarkable variability during the
 660 observation timespans. Furthermore, in all the datasets, the
 661 RFI is visibly limited in the bandwidth of ± 0.5 MHz. In
 662 case of low-power interference shown in Fig. 10d, the RFI
 663 is visible but its effect is not reflected on the scintillation
 664 index (S_4 index below the defined threshold). The dataset
 665 was kept and analyzed before being automatically discarded
 666 by the system in order to provide a term of comparison for
 667 more intense RFI phenomena. It is worth observing that the
 668 effects on S_4 , induced by RFI's PSD variations, are delayed of
 669 60 s due to the accumulation of I_p and Q_p samples over 60 s
 670 observation timespans. In Fig. 10a we observe intense power
 671 density fluctuations with an intensity peak (-5 dB-Hz) at about
 672 19:27:00. Two spectral lobes are visible in the first half of such
 673 a high-intensity interval. Fig. 10b shows a minimal intensity
 674 interferer where the aforementioned, peculiar spectral features
 675 are visible mostly between 00:18:00 and 00:20:00 and after
 676 00:22:00. Recorded power spectral density reached a peak of
 677 -15 dB Fig. 10c shows the most intense RFI action, where
 678 the received power reached a maximum in between -5 and
 679 0 dB - Hz in the interval between 01:08:00 and 01:10:00.
 680 Peak intensity caused spurious interference out of assumed

681 RFI bandwidth, being possibly detrimental for Galileo E1
 682 signals. Fig. 10d shows a fragmentation of the RFI power
 683 spectral density with an unusual behaviour and mid to low
 684 intensity sporadic peaks were observed in the second half of
 685 the dataset. Fig. 10e shows an increasing RFI intensity with
 686 time that reaches its maximum (-5 to 0 dB-Hz) by the end of
 687 the dataset. The dataset presents a unique example of regular
 688 intensity growth. Fig. 10f shows a sharp drop in the received
 689 RFI power density at about 05:45:30. The phenomenon sug-
 690 gests a sudden interruption of the RFI transmission. In the first
 691 quarter of the plot the PSD shows moderate to strong intensity
 692 in the range -10 to -5 dB-Hz. Additional Continuous wave
 693 (CW) interferences were sporadically observed, such as in
 694 Figs. 10d, 10e, and 10f with a non-negligible intensity at
 695 ± 0.5 MHz and ± 1.5 MHz. However, their presence cannot be
 696 directly related to the RFI target in this study. It is worth
 697 remarking that power variations highlighted by TFA appear
 698 slower than the changes observed in the spectral signature,
 699 thus we cannot assume they are related.

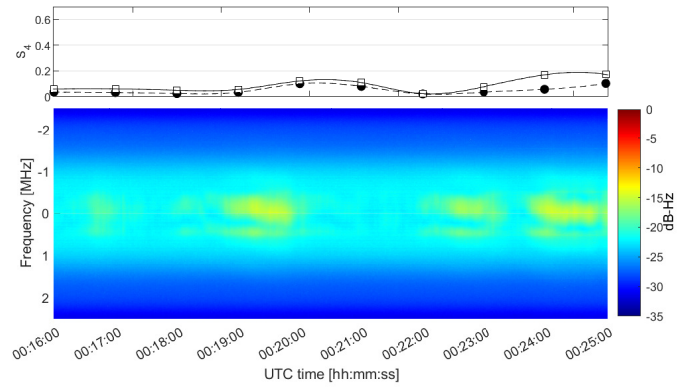
700 4) *C/N₀ estimation in GNSS receiver open-loop tracking*
 701 *stage:* According to the theoretical definitions of corrected
 702 amplitude ionospheric indices provided in Section II-B, the im-
 703 pact of rapid C/N_0 fluctuations induced by the RFI may cause
 704 misleading output values at GISTM. The following results
 705 show a more accurate match among such abrupt variations
 706 of the estimated C/N_0 and the anomalous increments of the
 707 corresponding amplitude scintillation index S_4 computed by
 708 the GISTM receiver. Noisy data series are obtained through
 709 (13) and they are plotted along with their 95 % confidence
 710 interval (shaded grey areas). The plots presented in Fig. 11,
 711 show the variation of the C/N_0 , namely $\delta C/N_0$, with respect
 712 to its mean estimated over non-overlapping windows of 60 s
 713 for the selected datasets. By comparing the results with the
 714 TFA analysis of Fig. 10, it can be seen that in correspondence
 715 of intense RFI occurrences, rapid fluctuations of the C/N_0 are
 716 present, thus they have not been properly compensated in the
 717 computation of $S_{4,n}$ through (7). Despite this effect is more
 718 evident for GPS L1/CA records, intense RFI occurrences also
 719 lead to remarkable fluctuations in Galileo E1c data³. More
 720 in detail: Fig. 11a shows the strongest fluctuations both in
 721 GPS and Galileo E1c signals. Peaks overcome a range of
 722 ± 5 dB up to severe drops of -8 dB for GPS L1/CA and
 723 confidence interval appears larger in correspondence of the

²Date and time are detailed in the subcaptions and data are limited to 9 minutes as 30 s are respectively discarded at the beginning and at the end of the data collection to avoid undesired transients.

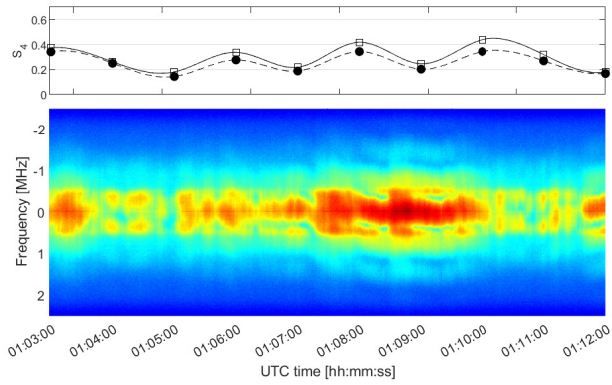
³ $\delta C/N_0$ and S_4 data series are obtained from independent devices



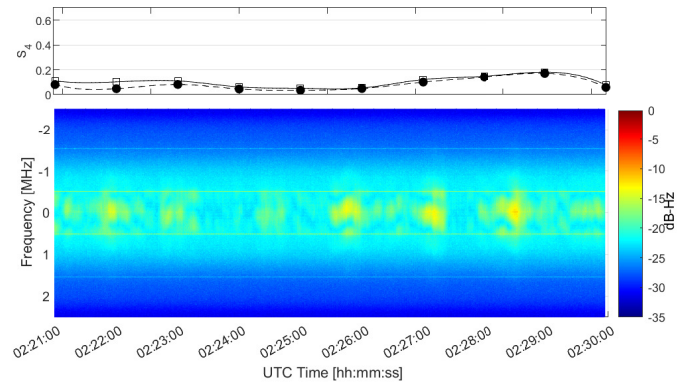
(a) 2021-09-16 19:22:24 UTC



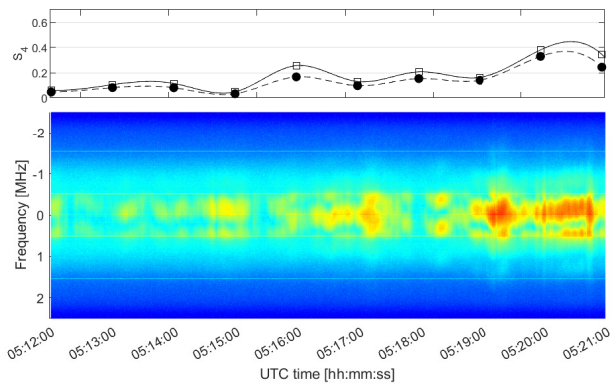
(b) 2021-09-17 00:15:40 UTC



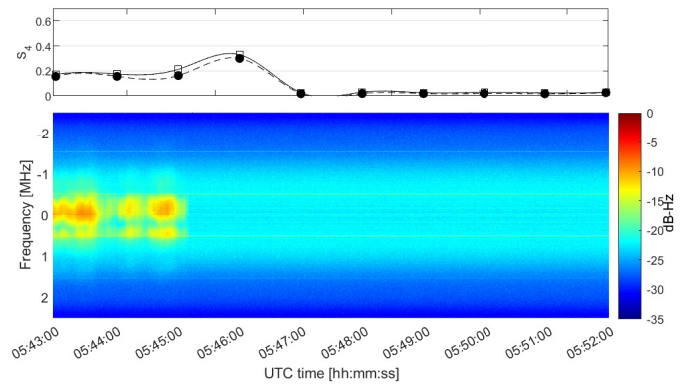
(c) 2021-09-18 01:02:41 UTC



(d) 2021-09-19 02:20:07 UTC



(e) 2021-09-19 05:12:02 UTC



(f) 2021-09-19 05:42:22 UTC

Fig. 10: TD-TFA of the datasets in Table III showing different RFI behaviours in terms of PSD time evolution, compared to maximum and mean S_4 time series (top panels). Filled and blank markers indicate mean and maximum S_4 values, respectively (top panels). Spectrograms and S_4 data series are obtained from independent devices.

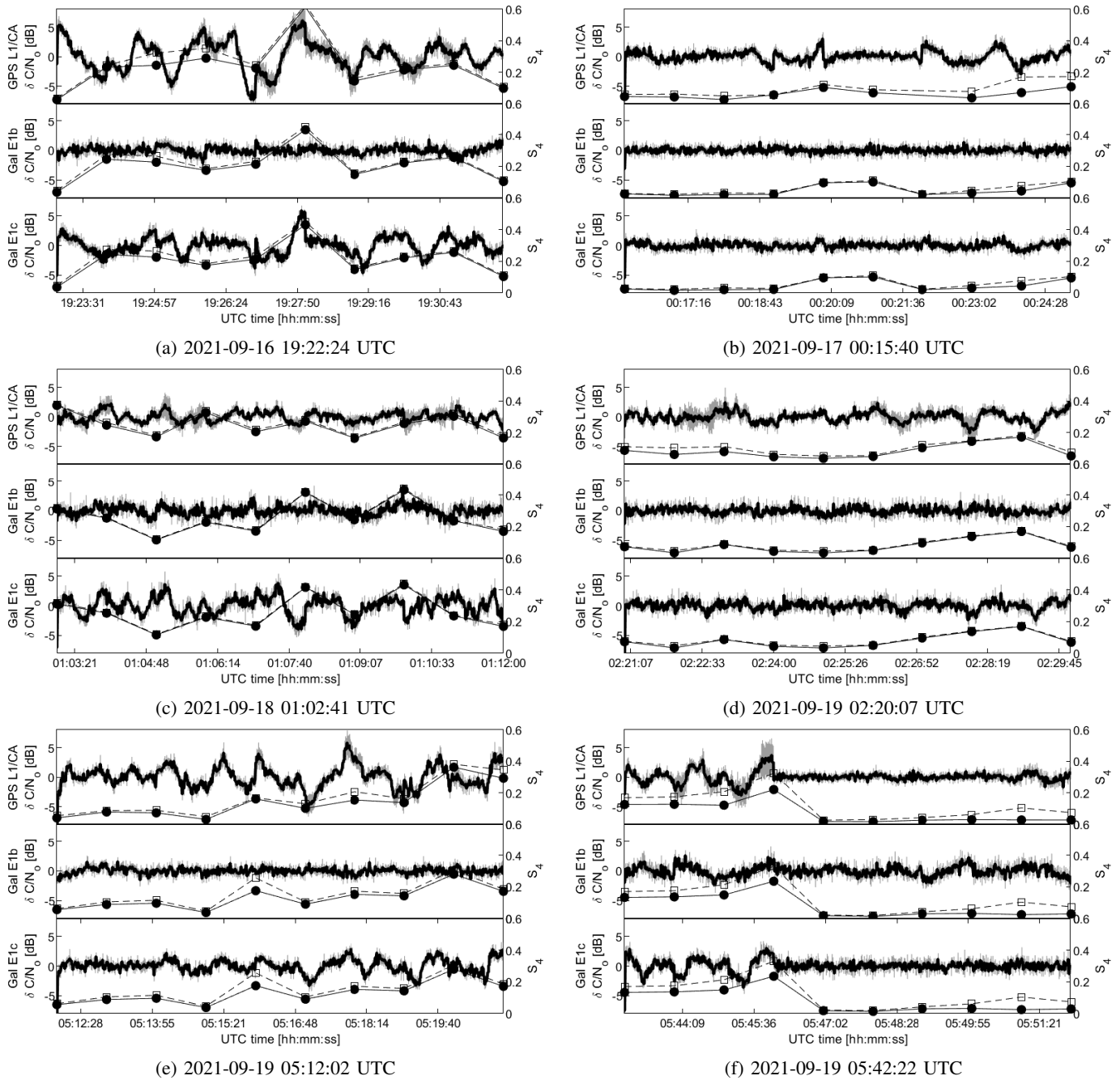


Fig. 11: Mean variation of the estimated C/N_0 (13) for GPS L1/CA, Galileo E1b and E1c during the observation timesteps of the selected datasets (limited to 9 minutes). Filled and blank markers indicate mean and maximum S_4 values, respectively (magnitude on the right y-axis). Background, grey-shaded areas show the 95% confidence interval (left y-axis).

724 main peak. Fig. 11b shows few fluctuations on GPS L1/CA
 725 C/N_0 estimates in the range of ± 3 dB. No relevant effects
 726 are observed on Galileo signals. The example confirms that
 727 low-intensity RFI may not severely impact S_4 estimation but
 728 they still induce perturbation in the estimated C/N_0 and may
 729 impact the performance of GNSS receivers. Fig. 11c shows
 730 intense fluctuations of Galileo E1c C/N_0 estimates in the
 731 range of ± 4 dB with remarkable C/N_0 drops reaching ap-
 732 proximately -5 dB between 01:07:00 and 01:09:00 UTC. GPS
 733 L1/CA C/N_0 estimates appear slightly affected in this case

but it shows a larger confidence interval in correspondence to
 the peak RFI intensity of Fig. 10c. This highlights a higher
 variability of the RFI effect on the different GNSS signals.
 Fig. 11d is a further example of poorly invasive RFI with
 constrained fluctuations in the range ± 3 dB. After 02:26:00
 UTC we observe a moderate increment of S_4 being reasonably
 attributed to the fluctuations in GPS L1/CA and Galileo E1c
 C/N_0 estimates. Fig. 11e shows increasing fluctuations of the
 $\delta C/N_0$ in both GPS L1/CA and Galileo E1c estimates. The
 strongest impact is visible for GPS L1/CA with values over-

734
 735
 736
 737
 738
 739
 740
 741
 742
 743

744 coming the range of ± 5 dB as well as remarkable enlargement
 745 of the confidence interval since about 05:16:00 UTC. Fig. 11f
 746 shows a sudden drop in the RFI intensity at about 05:46:00
 747 UTC. Such a peculiar behaviour was already shown in 10f,
 748 and it further clarify the direct effect of the RFI on the C/N_0
 749 estimation. S_4 reacts immediately to the quick fluctuations
 750 while assumes near-zero values by the end of the phenomenon.
 751 Until about 05:46:00 UTC both GPS L1/CA and Galileo E1c
 752 signals show severe fluctuations in the range of approximately
 753 ± 4 dB. The estimated average C/N_0 in GPS L1/CA also
 754 shows a larger confidence interval in correspondence of local
 755 maxima and minima.

756 **B. RFI Numerical Emulation**

757 Relying on the TD-TFA it can be inferred that no patterns
 758 can be recognized both in the temporal evolution of the signal
 759 and in its spectral content. Furthermore, RFI received power
 760 shows slow variations and a generous intensity range. TD-
 761 TFA was fundamental to observe that the RFIs occurrences
 762 may show a sharp starting and ending time that can be easily
 763 attributed to artificial, deliberate transmissions. Relying on
 764 these observations, the most relevant information that justify
 765 the modeling we propose hereafter comes from the persistence
 766 spectral analysis and from background literature on commu-
 767 nication systems and GNSS threats and mitigation. A basic
 768 model for a Multiple FSK (MFSK)/Frequency-Hopped (FH)
 769 signal was implemented to be compared with the identified
 770 RFI and foster the design of new countermeasures to mitigate
 771 its action. Despite of being a conventional modulation scheme
 772 for communication channels, MFSK has been employed in
 773 radar applications for its capacity of measuring and resolving
 774 targets in range and Doppler frequency simultaneously and un-
 775 ambiguously even in multitarget situations [62]. A MATLAB
 776 script was exploited to numerically evaluate the expression

$$x_{\text{RFI}}[n] \triangleq x_{\text{RFI}}(nT_s) = A \sum_{m=1}^W e^{j2\pi f_m(nT_s)nT_s} \quad (16)$$

777 where $f_m(nT_s)$ is a function that randomizes the generation of
 778 a set of m sub-tones included in a predefined frequency range,
 779 T_s is the sampling interval, A is the signal amplitude, and n
 780 is the discrete time index. The randomization of the sub-tones
 781 may reflect a set of random symbols carrying the data of an
 782 actual data transmission. The plot in Fig. 12 shows an example
 783 of a numerically-generated MFSK/FH jamming signal over a
 784 null-to-null bandwidth of about 1 MHz, by randomly switching
 785 among 10 sub-tones equally spaced in the range ± 0.5 MHz
 786 with an overall duration of 10 ms. Simulation settings are
 787 summarized in Table V for repeatability. It can be noticed
 788 that spectral estimation over longer observation time, e.g.
 789 10 ms, highlights the active sub-tones while shorter timespans
 790 prevent a detailed characterization of the spectral signature.
 791 By inducing a periodical change of the selected sub-tones,
 792 the signal would behave similarly to a randomized variant of
 793 a FH tick jammer described in [63], with a simpler spectral
 794 signature of the tones. The randomization of the tones allows
 795 to reduce autocorrelation and signal ergodicity. Discontinuities
 796 are hence introduced in the instantaneous frequency of the

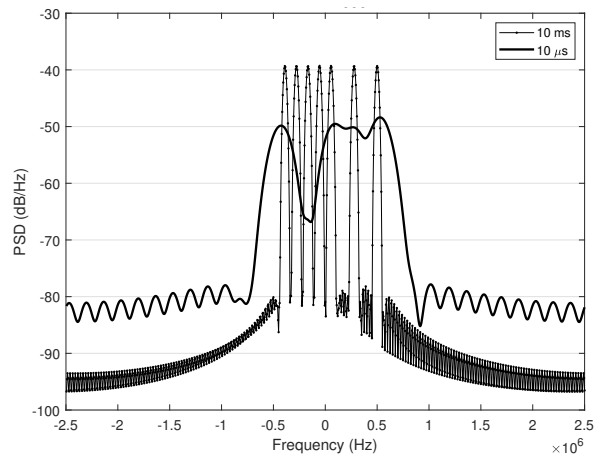


Fig. 12: PSDs of a simulated MFSK transmission observed over different snapshots duration and acting as an FH jamming interference. The spectral signature shows remarkable similarities with respect to the RFI's counterpart in Fig. 8 and Fig. 9. Lower noise floor is considered with respect to the collected data.

TABLE V: Simulation parameters for the emulation of a MFSK/FH jamming signal.

Symbol	Definition	Value
f_0	Center frequency	1575.42 MHz (L1)
f_s	Sampling frequency	5 Msps
T_x	Signal duration	10^{-3} s (10 ms)
M	Subcarriers	10
W	Random generation trials	3
R_f	Subcarriers range	± 0.5 MHz

797 jamming signals. Such discontinuities reduce the effectiveness
 798 of adaptive mitigation techniques based on adaptive filtering
 799 (e.g., adaptive notch filters), which may be unable to track the
 800 jamming signal. The designed MFSK signal shows frequent
 801 and remarkable changes in its spectral signature as shown in
 802 Fig. 13, where the numerical RFI shows a similar behaviour
 803 to the one observed in persistence spectra analysis of Fig. 9,
 804 in Section V.

805 **C. Impact of the RFI on scintillation data and filtering algo-**
 806 **rithm**

807 *1) Effects of the RFI on Low-latitudes ionospheric scin-*
 808 *tillations investigation:* As mentioned in Section I and III,
 809 mid-latitudes scintillation may occur as a consequence of
 810 disturbed space weather conditions; on the contrary, low-
 811 latitude scintillations are also possible during quiet time,
 812 especially for the geomagnetic latitudes close to the northern
 813 and southern EIA crests, due to the formation of small scale
 814 irregularities embedded in the EPBs. Considering the position
 815 of the Lampedusa observatory, an investigation addressed to
 816 the observation of low-latitude scintillations would require to
 817 also include the signals coming from low-elevation satellites
 818 with respect to the receiver FoV; this will introduce additional
 819 outliers in the data due to the effects of the multipath, as

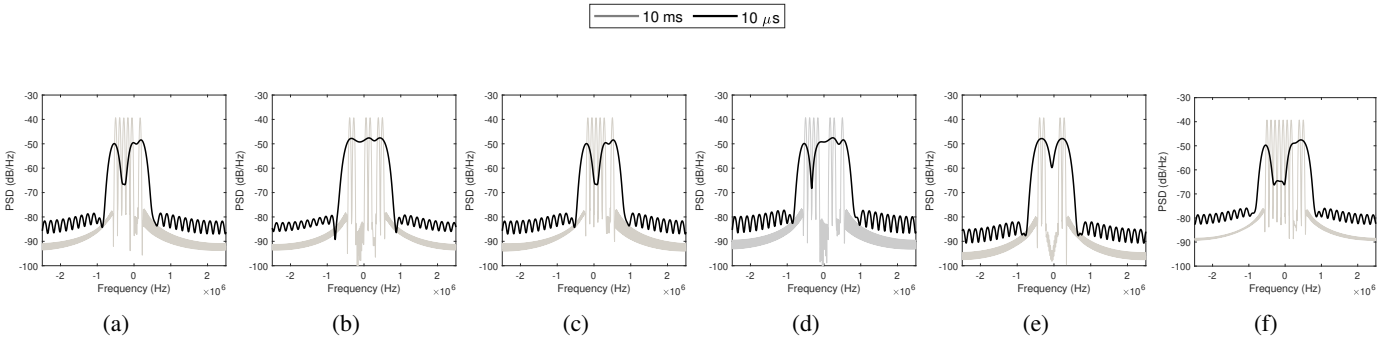


Fig. 13: Example of the evolution of the signal PSD of the emulated RFI. Different frequency resolutions are achieved by spectral estimation performed on different durations of the signal chunk under analysis, i.e., 10 ms (light-grey lines) and 10 μ s (black lines).

820 mentioned in Section III. In the analysis that follows, an
 821 elevation mask of 10° and an azimuthal mask between 90° and
 822 270° was applied to the signals in view, thus focusing on the
 823 middle and low-latitudes between 24.6°N and 36°N and on a
 824 longitudinal sector between 1°W and 26°E . The investigated
 825 time period goes from the 1th of July 2021 to the 31th
 826 October 2021, thus including the period of the equinox, when
 827 EPBs are more likely to occur. The considered signals are
 828 the one belonging to the GPS, Galileo, BDS and GLONASS
 829 constellations. The reported S_4 are the slant values calculated
 830 from the L1/E1 frequency band for each satellites in view at
 831 1-minute resolution.

832 According to the methodology described in Section IV-C1 ,
 833 the image of Fig. 14a shows the percentage occurrences of the
 834 S_4 index (S_{4POt}) above the threshold of moderate scintillation
 835 ($S_4 > 0.25$) on a bidimensional time-grid reporting the hour
 836 of the day in the horizontal axis and the day of the year
 837 in the vertical one. Each IPPs' epoch is converted in local
 838 time and the S_{4POt} are calculated according to (14) over
 839 the whole FoV under investigation and for time-intervals of
 840 4 minutes. In Fig. 14a the white line represents the solar
 841 terminator at 350 km (F-layer of the ionosphere), which may
 842 helps to identify post-sunset scintillation due to EPBs. As it is
 843 possible to see from Fig. 14a, two pronounced features are
 844 visible: the first one is due to the effect of the multipath,
 845 recognizable by the oblique stripes in the background due
 846 to the joint effect of the satellites' ground track, the fixed
 847 position of the reflecting obstacles and the time-difference
 848 between the solar and sidereal day. The second one consists
 849 in the brighter horizontal stripes, due to the effect of
 850 the RFI on the signals collected by the receiving antenna.
 851 Indeed, since the RFI affects the S_4 index of most of the
 852 satellites in view simultaneously (as shown in Section III), the
 853 anomalous occurrences can be recognized by looking at the
 854 highest values of the S_{4POt} in Fig. 14a, which suggest the
 855 presence of the interferer also in the data collected during the
 856 month of July and September (besides August, investigated
 857 in the preliminary analysis of Section III). Fig. 14b reports
 858 on a geographic map the percentage occurrences of the S_4
 859 (S_{4POs}) calculated according to (15) over the whole time-
 860 period under investigation and for geographic cells of $1^\circ \times$

861 1° spatial-resolution. The image of Fig. 14b shows that the
 862 entire FoV under investigation appears to have been subject
 863 to scintillations during the investigated time period; this is also
 864 a consequence of the RFI, which affect most of the signal in
 865 the FoV (see Section III). Instead, the stronger S_{4POs} values
 866 of Fig. 14b are mostly due to the multipath, which affect the
 867 signals coming from the low-elevation satellites.

868 Being not possible to exclude the low-elevation satellites
 869 (due to the necessity of observing low-latitudes), a possible
 870 way to remove the outliers produced by the multipath is
 871 by increasing the threshold of the S_4 occurrences above the
 872 level of severe scintillation ($S_4 > 0.7$); this operation has
 873 also the beneficial effect of removing the less intense S_4
 874 anomalies caused by the RFI, but will prevent the capability
 875 to detect possible real ionospheric scintillations events of
 876 moderate intensity. The result of this operation is shown in the
 877 images of Fig. 15: the background feature due to the multipath
 878 visible in Fig. 14a are removed (see Fig. 15a) and the overall
 879 spatial and temporal extent of the anomalies induced by the
 880 RFI is minimized as expected (see Fig. 15a and Fig. 15b in
 881 comparison to Fig. 14a and Fig. 14b).

882 2) *RFI filtering and detection of ionospheric scintillation*
 883 *events:* The S_4 percentage occurrences reported in Fig. 15
 884 are due to both RFI-affected observations and possibly actual
 885 ionospheric scintillation events. To finally detect and remove
 886 the remaining S_4 anomalies due to the severe effect induced
 887 by the RFI, it is possible to reprocess the original data according
 888 to the methodology reported in Section IV-C2. The result of
 889 this filtering operation is shown by the images of Fig. 16. By
 890 detecting and removing the occurrences attributed to the RFI,
 891 the timeline of the S_{4POt} reported in Fig. 16a allows to detect,
 892 without ambiguities, severe scintillation events (highlighted
 893 by the white dotted box) occurred in the post-sunset hours
 894 during the period of the autumn equinox 2021. Similarly,
 895 the map of Fig. 16b reports the S_{4POs} , showing the actual
 896 geographic area affected by scintillations (highlighted by the
 897 white dotted box) which cover the lowest latitudes in the
 898 FoV. The scintillation events highlighted in Fig. 16 reflect
 899 the typical features of ionospheric scintillations induced on
 900 GNSS signals by small scale irregularities embedded in EPBs
 901 reaching the north crest of the EIA. Even though an accurate

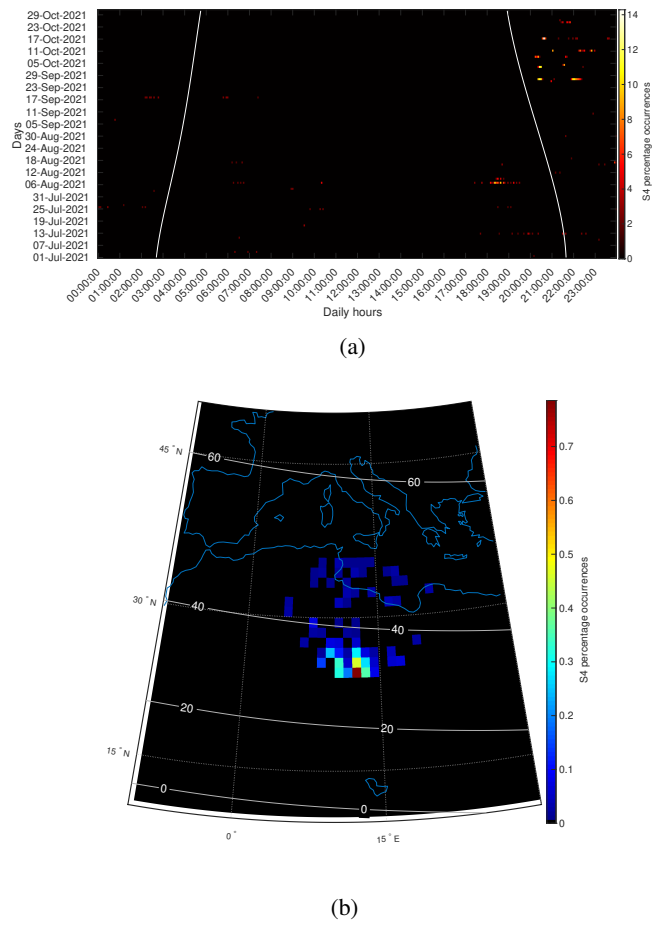
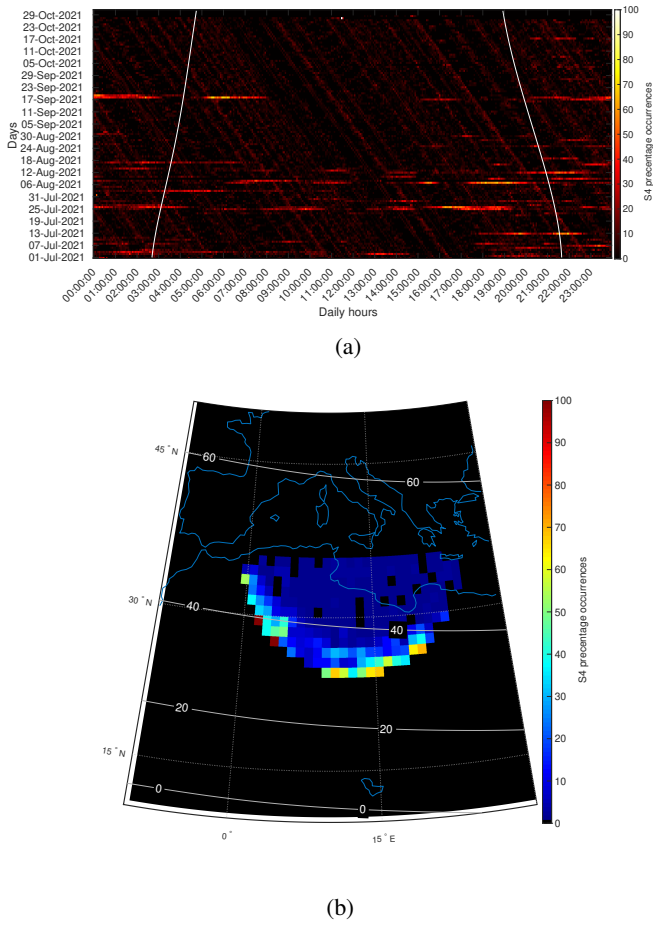


Fig. 14: S_{4POt} (Fig. 14a) and S_{4POs} (Fig. 14b) above the threshold of moderate scintillation ($S_4 > 0.25$) between July and October 2021. The white lines of Fig. 14a represents the solar terminator at 350 km. In Fig. 14b geographic coordinates are labeled at the border of the maps and represented by the dotted lines inside the map; geomagnetic latitudes are labeled inside the maps and represented with the continuous lines.

Fig. 15: S_{4POt} (Fig. 15a) and S_{4POs} (Fig. 15b) above the threshold of severe scintillation ($S_4 > 0.7$) between July and October 2021. The white lines of Fig. 15a represents the solar terminator at 350 km. In Fig. 15b geographic coordinates are labeled at the border of the maps and represented by the dotted lines inside the map; geomagnetic latitudes are labeled inside the maps and represented with the continuous lines.

VI. DISCUSSION

918

902 characterization of these phenomena falls outside the scope
 903 of this paper, the reported analysis allows to emphasize
 904 how unrecognized RFI would have triggered false scintillation
 905 alarms on several occasions (see Fig. 15a compared to
 906 Fig. 16a) and above incorrect locations (see Fig. 15b compared
 907 to 16b); this poses a threat for the reliability of real-time
 908 ionospheric scintillations monitoring application as well as for
 909 the integrity of scientific investigation addressed to ionospheric
 910 scintillation climatology. To conclude, the performances of the
 911 proposed filter are also highlighted in Fig. 17, which shows
 912 the result of the RFI-filtering operation before the mitigation
 913 of the multipath (data of Fig. 14), thus also including the
 914 anomalies causing moderate effect on ionospheric scintillation
 915 ($S_4 > 0.25$). The comparison between Fig. 17 and Fig. 14a
 916 highlights the capability of the procedures to effectively detect
 917 and remove the anomalies due to the interferer.

919 No natural events or human, licit or illicit activities being
 920 known to the authors seem related to the anomalous occur-
 921 rences and the features of the disturbance. Additionally, no
 922 other instruments were expected operating in GNSS L1-band
 923 at the ENEA station or can interfere by emitting spurious
 924 harmonics in such a frequency range. The RFI may be gener-
 925 ated in the proximity of the GISTM station (jamming or self-
 926 jamming) through a fixed or moving transmitter but the slow,
 927 yet remarkable power variations may indicate variable distance
 928 or heading of the transmitting antenna. This feature may be
 929 attributed to a moving transmitter carried on board of a plane,
 930 ground vehicle, or ship (mobile transmitter with fixed/moving
 931 antenna). Independently on the dynamics of the emitter, the
 932 RFI transmitting antenna may change its orientation along
 933 the time (e.g., fixed emitter with a spinning antenna as per
 934 radar applications). However, nor the regularity of the power
 935 fluctuation nor evident duty cycles in the received power

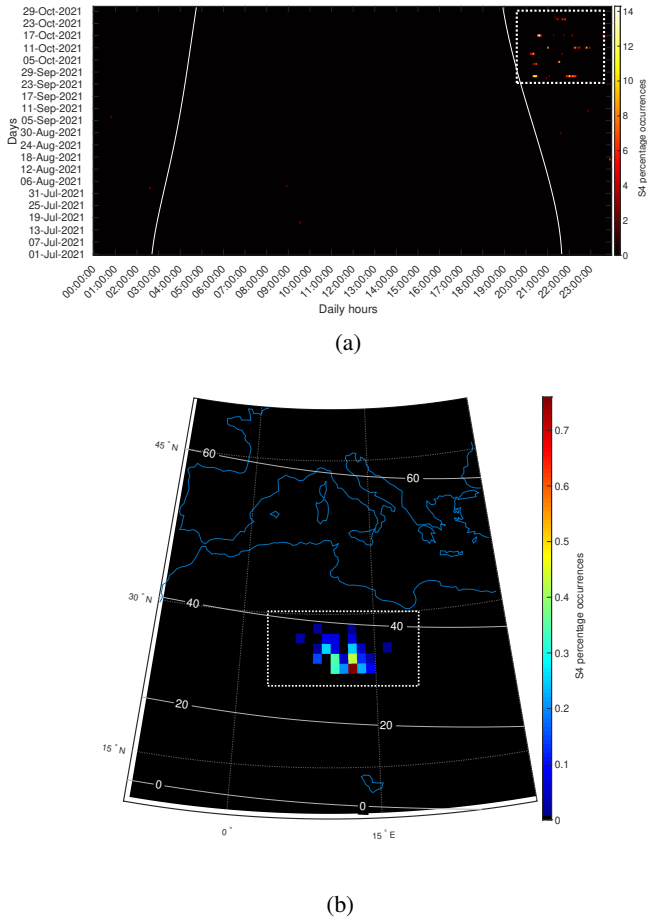


Fig. 16: S_{4POt} (Fig. 16a) and S_{4POs} (Fig. 16b) above the threshold of severe scintillation ($S_4 > 0.7$) between July and October 2021 after applying the filter for the RFI removal. The white lines of Fig. 16a represents the solar terminator at 350 km. In Fig. 16b geographic coordinates are labeled at the border of the maps and represented by the dotted lines inside the map; geomagnetic latitudes are labeled inside the maps and represented with the continuous lines. The white dotted boxes highlights ionospheric scintillation events due to EPBs.

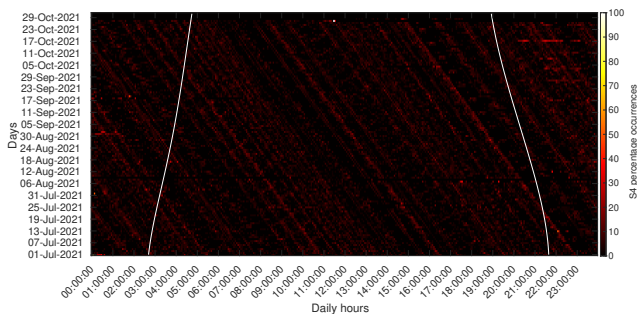


Fig. 17: S_{4POt} after applying the filter for RFI removal on the data of Fig. 14a.

suggest the possibility of a regularly spinning antenna. In light of this, the hypothesis of a moving emitter appears more reasonable. We cannot exclude the presence of jamming activities in the area of interest, as well as the possibility of experimental tests for MFSK radar systems or undocumented applications such as steganography in GNSS band for stealth data transmission. In fact, the characterization of the RFI detected in Lampedusa reflects the features of a deliberate MFSK transmission that may occasionally turn into a jamming interference on the L1/E1 frequency band in case of intense received signals. It mainly affects and severely degrades GPS L1/CA and Galileo E1c signals, but it seems poorly effective as a jammer against Galileo E1b, GLONASS and Beidou signals; in light of this, the gathered clues suggests the observed RFI may constitute a rough attempt of RF steganography covered by GNSS signals or a modern FH jammer. As a general remark, similar transmissions over GNSS L1/E1 center frequency are generally forbidden. However, while the United States (U.S.) prohibits unauthorized transmission on the GNSS frequency bands by federal laws [64], European regulations are more fragmented and may differ among member and non-member states. Specifically, the Italian legislation, with articles 340, 617, and 617 bis of the Penal Code, punishes the use and installation of jamming devices. In Italy, the deliberate use of interferers is allowed only to law enforcement and military forces, but the limitations at the continental border between Europe and Africa, such as in the area of Lampedusa, may not be exhaustively disciplined by regulations. Nonetheless, their occurrences are growing worldwide and at the European borders they might be due to the intensification of war actions and the presence of military enforcement. Therefore, an increasing attention is nowadays placed on their effects on several civil GNSS-related activities, such as flight operations, maritime navigation, critical infrastructures. A remarkable effort is indeed being placed towards RFI monitoring and localization by means of LEO satellites [44], [65]. From a terrestrial perspective, the deployment of multiple synchronous stations would allow as well for TDOA/FDOA-based interferer localization [66]–[68]. At the time of writing, RFI localization falls outside the scope of this article. Despite the interferer detected in Lampedusa is, at the moment, of unknown origin, its appearances during summer periods and the geopolitical conditions of the area make it possibly related to the migratory flows phenomena involving the surrounding seas, from the African coast to the east Mediterranean.

With regards to the scientific activities, recent discussions in the ionospheric community have raised the attention about the possible disruptive effects of RFIs on the data collected for scientific investigations of the ionosphere as well as for space weather monitoring applications. This paper provided an on-field proof of such vulnerabilities, showing the adverse impact of RFIs for both near-real time GNSS scintillation events detection as well as in case of climatological investigations of ionospheric scintillations. In the case of Lampedusa, the intensity and repetition over time of the S_4 anomalies allowed to promptly acknowledge the presence of a possible source of interference; however, similar but less impacting RFIs may not be easily recognizable and yet affecting the quality of the

936
937
938
939
940
941
942
943
944
945
946
947
948
949
950
951
952
953
954
955
956
957
958
959
960
961
962
963
964
965
966
967
968
969
970
971
972
973
974
975
976
977
978
979
980
981
982
983
984
985
986
987
988
989
990
991
992
993

collected data. At the same time, deploying capturing systems to detect and characterize RFIs, like the one presented in this study, is not a sustainable solution for both economical and technical aspects. At the time of writing, no real-time mitigation techniques for such elaborate interferers are known to the authors, and only a-posteriori processing may allow to detect interfered observations and provide quality metrics for the collected data. In this regard, this work proposed a preliminary post-processing methodology to detect and remove the RFI-induced anomalies from the scintillation data acquired by the GISTM receiver. The filter is not based on the specific characteristics of the RFI under investigation and, in principle, it can be also effective for different types of RFIs acting within the GNSS bandwidths; however, it has the bottleneck of being based on a threshold which is defined through a-priori assumptions and which is location-dependent. The design of more robust post-processing algorithms falls outside the scope of this paper and deserve dedicated investigations.

Summarizing, the lack of an accurate RFI model constitutes the main concern for a systematic analysis of its impact on the scintillation index. Besides, it is worth pointing out that a methodology to evaluate the RFI impact on the scintillation index is also lacking in the literature, and it deserves dedicated investigations in future works.

VII. CONCLUSIONS

This paper presented an investigation of a real scenario where an unclassified RFI affecting the GNSS signals jeopardize scientific activities like those carried-out by the INGV in the Mediterranean area of Lampedusa. It was shown that the computation of the ionospheric scintillation indices through modern commercial GISTM receivers may be misleading in those circumstances, thus triggering false ionospheric scintillation events and compromising the reliability of real-time monitoring applications as well as the quality of the data collected for scientific investigations. The analysis presented on the recorded GNSS signals specifically demonstrated that altered scintillation indices may be due to the non-stationarity of the estimated C/N_0 caused by the observed RFI. Further on-site campaigns are expected in the future by refining the experimental setup with a complete decoupling of the GISTM/SDR acquisition chain (e.g., antenna) and by implementing a multi-frequency acquisition unit (including L2/L5 GNSS bands). Moreover, by deploying multiple synchronous stations would allow to implement Time Difference of Arrival (TDOA)/Frequency Difference of Arrival (FDOA) interferer localization [66].

ACKNOWLEDGEMENTS

This investigation has been possible thanks to the National Agency for New Technologies, Energy, and Sustainable Economic Development (ENEA). In particular, we thank Alcide Giorgio di Sarra (scientific director of the activities at the ENEA Climate Observation Station) and Damiano Sferlazzo for providing us with the technical and logistical support during the measurements campaign and for the fruitful discussions. We acknowledge funding from the INGV research

project “Pianeta Dinamico, Theme 8 - ATTEMPT” (C.U.P. D53J19000170001) founded by the Italian Ministry of University and Research (“Fund aimed at relaunching the investments of central administrations of the state and the development of the country”, act 145/2018). A. Minetto acknowledges funding from the research contract no. 32-G-13427-5 DM 1062/2021 funded within the Programma Operativo Nazionale (PON) Ricerca ed Innovazione of the Italian Ministry of University and Research (MUR).

REFERENCES

- [1] P. Kintner, B. Ledvina, and E. De Paula, “GPS and ionospheric scintillations,” *Space weather*, vol. 5, no. 9, 2007.
- [2] L. Spogli, L. Alfonsi, G. De Franceschi, V. Romano, M. H. O. Aquino, and A. Dodson, “Climatology of GPS ionospheric scintillations over high and mid-latitude European regions,” *Annales Geophysicae*, vol. 27, no. 9, p. 3429–3437, Sep 2009. [Online]. Available: <http://dx.doi.org/10.5194/angeo-27-3429-2009>
- [3] R. S. Conker, M. B. El-Arini, C. J. Hegarty, and T. Hsiao, “Modeling the effects of ionospheric scintillation on GPS/Satellite-Based Augmentation System availability,” *Radio Science*, vol. 38, no. 1, p. 1–23, Jan 2003. [Online]. Available: <http://dx.doi.org/10.1029/2000RS002604>
- [4] N. Balan, L. Liu, and H. Le, “A brief review of equatorial ionization anomaly and ionospheric irregularities,” *Earth and Planetary Physics*, vol. 2, no. 4, p. 1–19, 2018. [Online]. Available: <http://dx.doi.org/10.26464/epp2018025>
- [5] H. Ghobadi, L. Spogli, L. Alfonsi, C. Cesaroni, A. Cicone, N. Linty, V. Romano, and M. Cafaro, “Disentangling ionospheric refraction and diffraction effects in GNSS raw phase through fast iterative filtering technique,” *GPS Solutions*, vol. 24, no. 3, Jun 2020. [Online]. Available: <http://dx.doi.org/10.1007/s10291-020-01001-1>
- [6] E. D. Kaplan and C. Hegarty, *Understanding GPS/GNSS: principles and applications*. Artech house, 2017.
- [7] L. Alfonsi, P. Cilliers, V. Romano, I. Hunstad, E. Correia, N. Linty, F. Dervis, O. Terzo, P. Ruiju, J. Ward *et al.*, “First observations of GNSS ionospheric scintillations from DemoGRAPE project,” *Space Weather*, vol. 14, no. 10, pp. 704–709, 2016.
- [8] J. Park, S. V. Veetil, M. Aquino, L. Yang, and C. Cesaroni, “Mitigation of ionospheric effects on GNSS positioning at low latitudes,” *NAVIGATION, Journal of the Institute of Navigation*, vol. 64, no. 1, pp. 67–74, 2017.
- [9] G. De Franceschi, L. Spogli, L. Alfonsi, V. Romano, C. Cesaroni, and I. Hunstad, “The ionospheric irregularities climatology over Svalbard from solar cycle 23,” *Scientific Reports*, vol. 9, no. 1, Jun 2019. [Online]. Available: <http://dx.doi.org/10.1038/s41598-019-44829-5>
- [10] C. Cesaroni, L. Spogli, L. Alfonsi, G. De Franceschi, L. Ciraolo, J. F. Galera Monico, C. Scotto, V. Romano, M. Aquino, and B. Bougard, “L-band scintillations and calibrated total electron content gradients over Brazil during the last solar maximum,” *Journal of Space Weather and Space Climate*, vol. 5, p. 11, 2015. [Online]. Available: <http://dx.doi.org/10.1051/swsc/2015038>
- [11] L. Spogli, C. Cesaroni, D. Di Mauro, M. Pezzopane, L. Alfonsi, E. Musicò, G. Povero, M. Pini, F. Dervis, R. Romero, N. Linty, P. Abadi, F. Nuraeni, A. Husin, M. Le Huy, T. T. Lan, T. V. La, V. G. Pillat, and N. Floury, “Formation of ionospheric irregularities over Southeast Asia during the 2015 St. Patrick’s Day storm,” *Journal of Geophysical Research: Space Physics*, vol. 121, no. 12, pp. 12,211–12,233, Dec 2016. [Online]. Available: <http://dx.doi.org/10.1002/2016JA023222>
- [12] O. Olwendo, C. Cesaroni, Y. Yamazaki, and P. Cilliers, “Equatorial ionospheric disturbances over the East African sector during the 2015 St. Patrick’s Day storm,” *Advances in Space Research*, vol. 60, no. 8, p. 1817–1826, Oct 2017. [Online]. Available: <http://dx.doi.org/10.1016/j.asr.2017.06.037>
- [13] L. Spogli, D. Sabbagh, M. Regi, C. Cesaroni, L. Perrone, L. Alfonsi, D. Di Mauro, S. Lepidi, S. A. Campuzano, D. Marchetti, A. Santis, A. Malagnini, C. Scotto, G. Cianchini, X. H. Shen, A. Piscini, and A. Ippolito, “Ionospheric response over Brazil to the August 2018 geomagnetic storm as probed by CSES-01 and swarm satellites and by local ground-based observations,” *Journal of Geophysical Research: Space Physics*, vol. 126, no. 2, Feb 2021. [Online]. Available: <http://dx.doi.org/10.1029/2020JA028368>

- [14] L. Alfonsi, C. Cesaroni, L. Spogli, M. Regi, A. Paul, S. Ray, S. Lepidi, D. Di Mauro, H. Haralambous, C. Oikonomou, P. R. Shreedevi, and A. K. Sinha, "Ionospheric disturbances over the Indian sector during 8 september 2017 geomagnetic storm: Plasma structuring and propagation," Mar 2021. [Online]. Available: <http://dx.doi.org/10.1029/2020SW002607>
- [15] C. Cesaroni, L. Alfonsi, M. Pezzopane, C. Martinis, J. Baumgardner, J. Wroten, M. Mendillo, E. Musicò, M. Lazzarin, and G. Umbriaco, "The first use of coordinated ionospheric radio and optical observations over Italy: Convergence of high-and low-latitude storm-induced effects," *Journal of Geophysical Research: Space Physics*, vol. 122, no. 11, Nov 2017. [Online]. Available: <http://dx.doi.org/10.1002/2017JA024325>
- [16] E. Afraimovich, E. Astafyeva, V. Demyanov, and I. Gamayunov, "Mid-latitude amplitude scintillation of GPS signals and GPS performance slips," *Advances in Space Research*, vol. 43, no. 6, pp. 964–972, 2009.
- [17] S. Vadakke Veetil, H. Haralambous, and M. Aquino, "Observations of quiet-time moderate midlatitude L-band scintillation in association with plasma bubbles," *GPS Solutions*, vol. 21, no. 3, p. 1113–1124, Jan 2017. [Online]. Available: <http://dx.doi.org/10.1007/s10291-016-0598-x>
- [18] K. Kauristie, J. Andries, P. Beck, J. Berdermann, D. Berghmans, C. Cesaroni, E. De Donder, J. de Patoul, M. Dierckxsens, E. Doornbos *et al.*, "Remote weather services for civil aviation—challenges and solutions," *Space Weather*, vol. 13, no. 18, p. 3685, 2021.
- [19] G. De Franceschi, L. Alfonsi, and V. Romano, "ISACCO: an Italian project to monitor the high latitudes ionosphere by means of GPS receivers," *GPS Solutions*, vol. 10, no. 4, pp. 263–267, 2006.
- [20] A. Van Dierendonck, J. Klobuchar, and Q. Hua, "Ionospheric scintillation monitoring using commercial single frequency C/A code receivers," in *proceedings of ION GPS*, vol. 93, 1993, pp. 1333–1342.
- [21] A. P. Cerruti, P. M. Kintner, D. E. Gary, L. J. Lanzerotti, E. R. de Paula, and H. B. Vo, "Observed solar radio burst effects on GPS/Wide Area Augmentation System carrier-to-noise ratio," *Space Weather*, vol. 4, no. 10, 2006. [Online]. Available: <https://agupubs.onlinelibrary.wiley.com/doi/abs/10.1029/2006SW000254>
- [22] H. Sato, N. Jakowski, J. Berdermann, K. Jiricka, A. Heßelbarth, D. Banyś, and V. Wilken, "Solar radio burst events on 6 September 2017 and its impact on GNSS signal frequencies," *Space Weather*, vol. 17, no. 6, pp. 816–826, 2019. [Online]. Available: <https://agupubs.onlinelibrary.wiley.com/doi/abs/10.1029/2019SW002198>
- [23] G. de Oliveira Nascimento Brassarote, E. M. de Souza, and J. F. G. Monico, "S4 index: does it only measure ionospheric scintillation?" *GPS Solutions*, vol. 22, no. 1, pp. 1–12, 2018.
- [24] G. D'Angelo, L. Spogli, C. Cesaroni, V. Sgrigna, L. Alfonsi, and M. Aquino, "GNSS data filtering optimization for ionospheric observation," *Advances in Space Research*, vol. 56, no. 11, p. 2552–2562, Dec 2015. [Online]. Available: <http://dx.doi.org/10.1016/j.asr.2015.10.002>
- [25] R. Romero and F. Dovis, "Towards analyzing the effect of interference monitoring in GNSS scintillation," in *Mitigation of Ionospheric Threats to GNSS*, R. Notarpietro, F. Dovis, G. D. Franceschi, and M. Aquino, Eds. Rijeka: IntechOpen, 2014, ch. 4. [Online]. Available: <https://doi.org/10.5772/58768>
- [26] —, "Effect of interference in the calculation of the amplitude scintillation index S4," in *2013 International Conference on Localization and GNSS (ICL-GNSS)*, 2013, pp. 1–6.
- [27] Y. Liao and Y. Zou, "Impact of radio frequency interference on GNSS ionospheric scintillation data analysis," in *2021 13th International Symposium on Antennas, Propagation and EM Theory (ISAPE)*, vol. Volume1, 2021, pp. 1–3.
- [28] F. Dovis, *GNSS interference threats and countermeasures*. Artech House, 2015.
- [29] Z. Zhang, Y. Qu, Z. Wu, M. J. Nowak, J. Ellinger, and M. C. Wicks, "RF steganography via LFM chirp radar signals," *IEEE Transactions on Aerospace and Electronic Systems*, vol. 54, no. 3, pp. 1221–1236, 2017.
- [30] Z. Zhang, M. J. Nowak, M. Wicks, and Z. Wu, "Bio-inspired RF steganography via linear chirp radar signals," *IEEE Communications Magazine*, vol. 54, no. 6, pp. 82–86, 2016.
- [31] B. Motella, S. Savasta, D. Margaria, and F. Dovis, "Method for assessing the interference impact on GNSS receivers," *IEEE Transactions on Aerospace and Electronic Systems*, vol. 47, no. 2, pp. 1416–1432, 2011.
- [32] S. Peng and Y. Morton, "A USRP2-based reconfigurable multi-constellation multi-frequency GNSS software receiver front end," *GPS Solutions*, vol. 17, no. 1, pp. 89–102, 2013.
- [33] G. Lachapelle and A. Broumandan, "Benefits of GNSS IF data recording," in *2016 European Navigation Conference (ENC)*, 2016, pp. 1–6.
- [34] N. Linty, F. Dovis, and L. Alfonsi, "Software-defined radio technology for GNSS scintillation analysis: bring Antarctica to the lab," *GPS Solutions*, vol. 22, no. 4, pp. 1–12, 2018.
- [35] N. Linty, F. Dovis, R. Romero, C. Cristodaro, L. Alfonsi, and E. Correia, "Monitoring ionosphere over Antarctica by means of a GNSS signal acquisition system and a software radio receiver," in *Proceedings of the 2016 International Technical Meeting of The Institute of Navigation*, 2016, pp. 549–555.
- [36] C. Ruf, S. Gross, and S. Misra, "RFI detection and mitigation for microwave radiometry with an agile digital detector," *IEEE Transactions on Geoscience and Remote Sensing*, vol. 44, no. 3, pp. 694–706, 2006.
- [37] J. R. Piepmeier, J. T. Johnson, P. N. Mohammed, D. Bradley, C. Ruf, M. Aksoy, R. Garcia, D. Hudson, L. Miles, and M. Wong, "Radio-frequency interference mitigation for the soil moisture active passive microwave radiometer," *IEEE Transactions on Geoscience and Remote Sensing*, vol. 52, no. 1, pp. 761–775, 2014.
- [38] P. N. Mohammed, M. Aksoy, J. R. Piepmeier, J. T. Johnson, and A. Bringer, "SMAP L-band microwave radiometer: RFI mitigation prelaunch analysis and first year on-orbit observations," *IEEE Transactions on Geoscience and Remote Sensing*, vol. 54, no. 10, pp. 6035–6047, 2016.
- [39] F. Ticoni, C. Anderson, J. Figa-Saldaña, J. J. W. Wilson, and H. Bauch, "Analysis of radio frequency interference in metop ASCAT backscatter measurements," *IEEE Journal of Selected Topics in Applied Earth Observations and Remote Sensing*, vol. 10, no. 5, pp. 2360–2371, 2017.
- [40] E. Pica, C. Marocci, C. Cesaroni, E. Zuccheretti, M. Pezzopane, S. Vecchi, V. Romano, and L. Spogli, "The SWIT-eSWua system: managing, preservation and sharing of the historical and near real-time ionospheric data at the INGV," in *American Geophysical Union (AGU) 2020 Fall Meeting*, Mar 2021. [Online]. Available: <http://dx.doi.org/10.1002/essoar.10506618.1>
- [41] G. Garelli and M. Tazzioli, "The EU hotspot approach at Lampedusa," *Open Democracy*, vol. 26, 2016.
- [42] E. Pulitano, *Island(s): Lampedusa as a "Hotspot" of EU Border Policies*. Cham: Springer International Publishing, 2022, pp. 43–73. [Online]. Available: https://doi.org/10.1007/978-3-031-05992-6_3
- [43] A. I. U. Eurocontrol, "Does radio frequency interference to satellite navigation pose an increasing threat to network efficiency, cost-effectiveness and ultimately safety?" Tech. Rep, Tech. Rep., 2021.
- [44] T. M. Roberts, T. K. Meehan, J. Y. Tien, and L. E. Young, "Detection and localization of terrestrial L-band RFI with GNSS receivers," *IEEE Transactions on Geoscience and Remote Sensing*, vol. 60, pp. 1–11, 2022.
- [45] N. Linty, A. Minetto, F. Dovis, and L. Spogli, "Effects of phase scintillation on the GNSS positioning error during the september 2017 storm at Svalbard," *Space Weather*, vol. 16, no. 9, pp. 1317–1329, 2018.
- [46] C. Cristodaro, F. Dovis, N. Linty, and R. Romero, "Design of a configurable monitoring station for scintillations by means of a GNSS software radio receiver," *IEEE Geoscience and Remote Sensing Letters*, vol. 15, no. 3, pp. 325–329, 2018.
- [47] P. Misra and P. Enge, "Global positioning system: Signals," *Measurements and Performance*, pp. 381–384, 2006.
- [48] M. Pini, E. Falletti, and M. Fantino, "Performance evaluation of C/N0 estimators using a real time GNSS software receiver," in *2008 IEEE 10th International Symposium on Spread Spectrum Techniques and Applications*, 2008, pp. 32–36.
- [49] L. Alfonsi, L. Spogli, G. De Franceschi, V. Romano, M. Aquino, A. Dodson, and C. N. Mitchell, "Bipolar climatology of GPS ionospheric scintillation at solar minimum," *Radio Science*, vol. 46, no. 03, pp. 1–21, 2011.
- [50] U. atmosphere physics radiopropagation Working Group, C. Cesaroni, G. De Franceschi, C. Marocci, E. Pica, V. Romano, and L. Spogli, "Electronic space weather upper atmosphere database (eSWua) - GNSS scintillation data, version 1.0," 2020.
- [51] F. S. Rodrigues, J. G. Socola, A. O. Moraes, C. Martinis, and D. A. Hickey, "On the properties of and ionospheric conditions associated with a mid-latitude scintillation event observed over southern united states," Jun 2021. [Online]. Available: <http://dx.doi.org/10.1029/2021SW002744>
- [52] B. M. Ledvina, J. J. Makela, and P. M. Kintner, "First observations of intense GPS L1 amplitude scintillations at midlatitude," pp. 4–1–4–4, Jul 2002. [Online]. Available: <http://dx.doi.org/10.1029/2002GL014770>
- [53] N. Balan, K. Shiokawa, Y. Otsuka, S. Watanabe, and G. J. Bailey, "Super plasma fountain and equatorial ionization anomaly during penetration electric field," pp. n/a–n/a, Mar 2009. [Online]. Available: <http://dx.doi.org/10.1029/2008JA013768>
- [54] D. Di Mauro, M. Regi, S. Lepidi, A. Del Corpo, G. Dominici, P. Bagiacchi, G. Benedetti, and L. Cafarella, "Geomagnetic activity

1271 at Lampedusa island: Characterization and comparison with the other
 1272 Italian observatories, also in response to space weather events,” *Remote*
 1273 *Sensing*, vol. 13, no. 16, p. 3111, Aug 2021. [Online]. Available:
 1274 <http://dx.doi.org/10.3390/rs13163111>
 1275 [55] P. Bagiacchi, G. Benedetti, L. Cafarella, D. Di Mauro, and A. E.
 1276 Zirizzotti, “The new system for data acquisition and visualisation of the
 1277 magnetic field of the Earth,” *Rapporti Tecnici INGV*, vol. 428, Feb 2021.
 1278 [Online]. Available: <http://editoria.rm.ingv.it/rapporti/2021/rapporto428/>
 1279 [56] J. Uwamahoro and J. Habarulema, “Empirical modeling of the storm
 1280 time geomagnetic indices: a comparison between the local K and
 1281 global Kp indices,” *Earth, Planets and Space*, vol. 66, no. 1, p. 95,
 1282 2014. [Online]. Available: <http://dx.doi.org/10.1186/1880-5981-66-95>
 1283 [57] L. Spogli, H. Ghebadi, A. Cicone, L. Alfonsi, C. Cesaroni, N. Linty,
 1284 V. Romano, and M. Cafaro, “Adaptive phase detrending for gnss
 1285 scintillation detection: A case study over antarctica,” p. 1–5, 2022.
 1286 [Online]. Available: <http://dx.doi.org/10.1109/LGRS.2021.3067727>
 1287 [58] P. Welch, “The use of fast Fourier transform for the estimation of power
 1288 spectra: A method based on time averaging over short, modified peri-
 1289 odograms,” *IEEE Transactions on Audio and Electroacoustics*, vol. 15,
 1290 no. 2, pp. 70–73, 1967.
 1291 [59] M. H. Hayes, *Statistical digital signal processing and modeling*. John
 1292 Wiley & Sons, 2009.
 1293 [60] F. J. Harris, “On the use of windows for harmonic analysis with the
 1294 discrete Fourier transform,” *Proceedings of the IEEE*, vol. 66, no. 1, pp.
 1295 51–83, 1978.
 1296 [61] L. Cohen, *Time-frequency analysis*. Prentice hall New Jersey, 1995,
 1297 vol. 778.
 1298 [62] M. Kronauge and H. Rohling, “New chirp sequence radar waveform,”
 1299 *IEEE Transactions on Aerospace and Electronic Systems*, vol. 50, no. 4,
 1300 pp. 2870–2877, 2014.
 1301 [63] D. Borio and C. Gioia, “Mitigation of frequency-hopped tick jamming
 1302 signals,” in *2020 IEEE/ION Position, Location and Navigation Symposi-
 1303 um (PLANS)*, 2020, pp. 624–630.
 1304 [64] F. C. Commission, “Enforcement advisory: Warning: Jammer use is
 1305 prohibited; prohibition applies to use by the public and state and local
 1306 government agencies,” 2014.
 1307 [65] M. J. Murrian, L. Narula, P. A. Iannucci, S. Budzien, B. W. O’Hanlon,
 1308 M. L. Psiaki, and T. E. Humphreys, “First results from three years
 1309 of GNSS interference monitoring from low earth orbit,” *Navigation*,
 1310 vol. 68, no. 4, pp. 673–685, 2021.
 1311 [66] N. O’Donoghue, *Emitter Detection and Geolocation for Electronic
 1312 Warfare*. Artech House, 2019.
 1313 [67] K. Becker, “An efficient method of passive emitter location,” *IEEE
 1314 Transactions on Aerospace and Electronic Systems*, vol. 28, no. 4, pp.
 1315 1091–1104, 1992.
 1316 [68] A. G. Dempster and E. Cetin, “Interference localization for satellite
 1317 navigation systems,” *Proceedings of the IEEE*, vol. 104, no. 6, pp. 1318–
 1318 1326, 2016.



Alex Minetto (GS’17-M’20) was born in Pinerolo, Italy, in 1990. He received the B.Sc. and M.sc. degrees in Telecommunications Engineering from Politecnico di Torino, Turin, Italy and his Ph.D. degree in Electrical, Electronics and Communications Engineering, in 2020. He joined the Department of Electronics and Telecommunications of Politecnico di Torino in 2022 as researcher and assistant professor. His current research interests cover navigation signal design and processing, advanced Bayesian estimation applied to Positioning and Navigation Technologies (PNT) and applied Global Navigation Satellite System (GNSS) to space weather and space PNT.



Claudio Cesaroni is Researcher at INGV and Responsible of the Upper Atmosphere Physics and Radiopropagation Unit. He is expert in ionospheric physics, in data analysis and treatment techniques focused on TEC calibration technique and effects of spatial and temporal gradients on GNSS signals. He developed algorithms for the analysis of TEC gradients and scintillations data at low latitudes and for the analysis of the dynamics of the ionospheric irregularities. He was also involved in the IPS project and in the PECASUS consortium for the development of models and tools to nowcast and forecasting TEC gradients effects on GNSS signals. He took part to several Antarctic and Arctic scientific expeditions. He is author of an international patent: Grzesiak M, Cesaroni, C., Spogli, L., De Franceschi, G. “Method for forecasting ionosphere total electron content and/or scintillation parameters”, International Publication Number WO 2016/185500 A1.



Fabio Dovis (GS’98-M’01) was born in Bruino, Italy, in 1970. He received his M.Sc. degree in 1996 and his Ph.D. degree in 2000, both from Politecnico di Torino, Turin, Italy. He joined the Department of Electronics and Telecommunications of Politecnico di Torino as an assistant professor in 2004 and as associate professor in 2014. Since 2021 he is a full professor in the same department where he coordinates the Navigation Signal Analysis and Simulation (NavSAS) research group. He has a relevant experience in European projects in satellite navigation as well as cooperation with industries and research institutions. He serves as a member of the IEEE Aerospace and Electronics Systems Society Navigation Systems Panel. His research interests cover the design of GPS and Galileo receivers and advanced signal processing for interference and multipath detection and mitigation, as well as ionospheric monitoring.



Emanuele Pica is a technologist at Istituto Nazionale di Geofisica e Vulcanologia (INGV), Rome, Italy. He received a B.Sc degree in Electronic Engineering from University of Salerno, Salerno, Italy and a M.sc. degree in Space and Astronautical Engineering from Sapienza University, Rome, Italy. His research activities cover the fields of research data management, research infrastructures and ionospheric monitoring. He is currently responsible for the INGV ionospheric scintillations network.